VARIABILITY OF STRAIN AND STRAIN RATE IN THE HUMAN TIBIAL DIAPHYSIS DURING WALKING

by

Tyler Franklin Rooks

A thesis

submitted in partial fulfillment

of the requirements for the degree of

Master of Science in Mechanical Engineering

Boise State University

August 2011

BOISE STATE UNIVERSITY GRADUATE COLLEGE

DEFENSE COMMITTEE AND FINAL READING APPROVALS

of the thesis submitted by

Tyler Franklin Rooks

Thesis Title: Variability of Strain and Strain Rate in the Human Tibial Diaphysis During Walking

Date of Final Oral Examination: 06 May 2011

The following individuals read and discussed the thesis submitted by student Tyler Franklin Rooks, and they evaluated his presentation and response to questions during the final oral examination. They found that the student passed the final oral examination.

Kotaro Sasaki, Ph.D.	Co-Chair, Supervisory Committee
Eric L. Dugan, Ph.D.	Co-Chair, Supervisory Committee
Michelle Sabick, Ph.D.	Member, Supervisory Committee

The final reading approval of the thesis was granted by Kotaro Sasaki, Ph.D., and Eric L. Dugan, Ph.D., Co-Chairs of the Supervisory Committee. The thesis was approved for the Graduate College by John R. Pelton, Ph.D., Dean of the Graduate College.

ACKNOWLEDEMENTS

I would like to thank my thesis advisor Dr. Kotaro Sasaki for all of his help while I was a student at Boise State University (BSU). He was instrumental in the research and writing processes. The different perspective he provided was very helpful in filling in gaps and furthering my understanding of both writing styles and research methods. I would also like to thank the remaining members of my thesis committee, Dr. Eric Dugan and Dr. Michelle Sabick, for all of their help and patience throughout this process. Additionally, I am very thankful for all of the help Dan Leib provided throughout the research process. Without his help and guidance, I would not have been able to complete all of the research. Finally, I would like to express my gratitude to all of the researchers at Ball State University's BIOMECHANICS LAB for collecting and processing the experimental data used for this study.

AUTOBIOGRAPHICAL SKETCH OF THE AUTHOR

Tyler Rooks graduated from Colorado School of Mines (CSM) in Golden, CO with a BS in Engineering with a mechanical specialty in May 2009. Upon completion of his BS degree at CSM, he enrolled in the Mechanical Engineering Master of Science program at Boise State University (BSU). While not attending school, he spent time volunteering in the Musculoskeletal Disorders laboratory at the University of Colorado's School of Medicine (Denver, CO) in the summers while at CSM. While at BSU, he spent time away from school as a fellow for the Oak Ridge Institute of Science and Engineering (ORISE) at Fort Rucker in Alabama. Following completion of the requirements for a Master of Science in Mechanical Engineering degree, he plans to return and complete the remaining time available as a fellow for ORISE.

ABSTRACT

With the prevalence of stress fractures in the military and athletes of all levels, research into the pathology of this injury has taken flight in recent years. One area of research has focused on the role bone strain, which is known to be a factor in bone remodeling, has on stress fracture development. It has been difficult to perform studies in this area of research due to the invasiveness of *in vivo* measurements of the bone strain. Recently, a methodology for approximating the bone strain using a computational model was proposed by Al Nazer *et al.* (Al Nazer et al., 2008b). This methodology employs the combination of a dynamic simulation with a flexible body (finite element model), replacing one of the rigid bodies in the musculoskeletal model. The use of a flexible body, generated from the deformation modes of the bone, sufficiently decreases the degrees of freedom of the finite element model so that it can be used in a fully dynamic simulation. This study used a similar methodology, with an improved methodology for generating the flexible tibia, to establish a normative range of strains seen in a homogenous population of young, healthy, male subjects. The flexible tibia was generated by first segmenting the CT scanned tibia to regenerate a 3D solid model of the tibia geometry, then applying the material properties developed from the CT scan Hounsfield Units (HU) values for each element in the finite element model, and finally performing a modal analysis on the finite element model to generate the deformation modes of the tibia model. Strain data from five reference locations around the tibial mid-shaft, and a simulated staple were obtained using subject-specific forward dynamics simulations. The results showed large variability in strain magnitude for a homogenous population. The mean peak and standard deviation for the maximum principal strain, minimum principal strain, and maximum shear strain for the anterior-

medial location were 488με (±175 με), -473με (±93με), and 814με (±177με), respectively. However, comparisons with previous *in vivo* research showed that nearly all *in vivo* data were within two standard deviations of the mean values. The ability to differentiate between normal and potentially harmful strain levels is key to determining their effect on stress fracture development.

TABLE OF CONTENTS

LIST OF TABLES

LIST OF FIGURES

CHAPTER 1: INTRODUCTION

1.1 Background

Mechanical failure of bone can be categorized into two failure mechanisms. The first mechanism involves a single traumatic loading event that generates strains above the failure load of bone causing a fracture. The second mechanism is characterized by the buildup of microdamage (microscopic scale breakdown of bone) resulting from repetitive loading at subultimate strains and causing a stress fracture. Prior to a stress fracture, the bone will go through a stress reaction, which is characterized by microfailures in the bone that have yet to disrupt the cortical bone (Kaeding & Najarian, 2010). This type of fracture is often diagnosed in athletes of all levels and military recruits, with incidence reports of 0.2% to 4% for males and 1% to 7% for females in the US military, and up to 31% in track and field sports (Burr et al., 1996; Martin, 2001). While stress fractures can occur in nearly any bone, the most common sites are the lower extremities, with the tibia accounting for up to 50% of all stress fractures (Kaeding & Najarian, 2010; Whiting & Zernicke, 1998).

According to Wolff's Law, bone remodels itself to adapt to applied stresses (Takeda, Narita, & Ito, 2004). Over the years, this theory has been adapted extensively. Early studies showed that the state of strain, rather than stress, drives bone adaptation (Thompson, 1961), and that there is a "minimum effective strain" that must be exceeded to stimulate that adaptation (Frost, 1964). More recent studies have shown that bone growth is influenced by dynamic strain rather than static strain (Lisková & Hert, 1971), is proportional to the peak applied strain (Lanyon, Hampson, Goodship, & Shah, 1975), and that the frequency of loading effects bone remodeling (Rubin & McLeod, 1994). During the process of bone remodeling, if the magnitude

or frequency of the applied load exceeds the ability of bone to remodel, stress reactions or fractures may develop (Whiting & Zernicke, 1998). As discussed previously, the buildup of microdamage (microcracks) in the bone leads to stress reactions, which can end up causing stress fractures. Recent studies investigating the dependence of bone material properties on the strain rate have shown that the material properties of bone change with changes in strain rate (Hansen, Zioupos, Simpson, Currey, & Hynd, 2008; Zioupos, Hansen, & Currey, 2008). Additionally, Zioupos e*t al*. found that the formation of microcracks was inversely proportional to the strain rate applied, showing that lower strain rates resulted in a larger amount of microcracks in the bone (Zioupos et al., 2008). With the dependence of bone remodeling on strain and the relationship between strain rate and microcrack formation, the ability to quantify this strain and strain rate is very important for studying bone remodeling processes and stress fracture development.

1.2 Determining Bone Strain

1.2.1 *In Vivo* Strain Measurement

Direct *in vivo* measurements have been used to observe how bone strain changes in the tibia under different external conditions, including overground vs. treadmill running (C. Milgrom et al., 2003), the effect of shoe orthoses on stress fracture prevention (I. M. Ekenman et al., 2002), and the effect of cane use on tibial strain and strain rates (Mendelson et al., 1998). In addition to investigating these external conditions, researchers have also investigated the effects of activity level (Burr et al., 1996) and fatigue (Fyhrie et al., 1998; C. Milgrom et al., 2007) on bone strain and stress fractures. However, *in vivo* studies have several limitations. First, the instrumentation of strain gauges or strain gauge staples is extremely invasive and therefore experiments using human subjects are difficult to conduct. Second, the reliability of the instrumentation appears low. *In vivo* strain gauge instrumentation is difficult, with many uncertainties associated with bonding

and bone preparation (C. Milgrom et al., 2004) and a susceptibility to motion artifact (Fyhrie et al., 1998). Ekenman *et al.* found that there was a low inter-subject reliability for both strain gauges and strain gauge staples (I. Ekenman, Halvorsen, Westblad, Felländer-Tsai, & Rolf, 1998). Finally, the extent of the area the strain gauge instrumentation can provide information about is low. *In vivo* strain gauge measurements can only determine the strain in a limited area around the instrumented site (I. Ekenman et al., 1998). Currently, there is not an experimental solution to these problems.

1.2.2 Computational Approach

Computational models combining a musculoskeletal simulation and finite element (FE) models provide an alternative approach to *in vivo* measurements that is capable of approximating the bone strain during dynamic motor activities. The advantages of a computational approach include: minimal invasiveness, allowing researchers to recruit more participants, elimination of the errors associated with implanting the strain gauges, and the capability of providing strain distributions from anywhere in the tibia. A recent computational approach using musculoskeletal models with a bone (tibia) modeled as a flexible body, in place of a rigid body, has shown promising results of estimating tibial bone strains and strain rates during dynamic human movements such as walking (Al Nazer et al., 2008a; Al Nazer, Rantalainen, Heinonen, Sievänen, & Mikkola, 2008b; Klodowski, Rantalainen, Mikkola, Heinonen, & Sievanen, 2009). The main advantage of using a flexible bone is to reduce the large computational cost required for a finite element analysis to compute bone strain. Typically, three-dimensional bone models have very large nodal degrees of freedom (DOF) due to bone's complex geometry. These large nodal DOF make static and dynamic finite element solutions computationally expensive. This flexible body approach reduces the number of nodal DOF using a Craig-Bampton modal analysis (Craig & Bampton, 1968), which takes into account only the most important deformation modes based on

the natural frequencies of the bone. Through the combination of internal dynamic and boundary static modes, the Craig-Bampton modal analysis can accurately model the deformation of a complex system (geometry) with a significant reduction in the number of DOF (Gerstmayr & Ambrosio, 2007).

In the finite element (FE) modeling of bones, regenerating accurate geometry and applying the material properties are very important steps and have been researched extensively (Gray, Zavatsky, Cristofolini, & Gill, 2008; Lengsfeld, Schmitt, Alter, Kaminsky, & Leppek, 1998; Rathnayaka, Sahama, Schuetz, & Schmutz, 2010; Schileo, Taddei, Malandrino, Cristofolini, & Viceconti, 2007; Taddei, Schileo, Helgason, Cristofolini, & Viceconti, 2007). Subject specific bone geometry can be regenerated from medical imaging data such as Computed Tomography (CT) scans and Magnetic Resonance Imaging (MRI). The advantage of CT scans, over MRI, is that in addition to bone geometry, bone material properties (apparent density) can be estimated. The apparent density is used to calculate subject specific Young's modulus (E) for the bone. With the variety of bone density – Young's Modulus relationships that have been proposed for different bones (femur, vertebra, and tibia) and bone types (cortical and trabecular), the options for which relationship to use depend on which bone(s) and what type(s) of bone are of interest.

1.3 Tibial Bone Strain While Walking

Walking is one of the most common dynamic motor activities, and a variety of kinesiological studies have been reported. However, the strain state of the tibia, during walking is not well understood. An understanding of the tibial strain state during walking may provide important implications for understanding the mechanisms of stress fracture development, developing rehabilitation protocols after fracture occurs, or serving as a basis for comparisons between various dynamic motor activities such as running.

In vivo measurements of bone strain have been a topic of study for many years, beginning with Lanyon *et al.* in 1975. They compared the strain state of the tibia for a single subject while walking with and without shoes on a treadmill and walking overground with four loading conditions. For the condition of walking on a treadmill with shoes, they found a peak maximum principal strain of 311 microstrain (με), a peak minimum principal strain of -368με, and a maximum strain rate of $-3.37X10^{3}$με/sec (Lanyon et al., 1975). Several similar studies investigating the strain state of the tibia under varying conditions have since been performed. Burr *et al.* investigated the effects of activity levels on the tibial bone strain, including walking and running (Burr et al., 1996). For the condition of walking on level ground, they found slightly higher maximum and minimum principal strains of 437με and -544με, respectively (Burr et al., 1996). More recently, Milgrom *et al.* reported strains of 394με (maximum tensile strain) and -672με (maximum compressive strain) for the tibia (C. Milgrom et al., 2007).

There are only a few studies examining tibial strains during walking using computational approaches (Al Nazer et al., 2008a; Klodowski et al., 2009). Al Nazer *et al.* obtained tibial strains using a flexible model of the tibia within a musculoskeletal model (Al Nazer et al., 2008a). The strains calculated in this study were in general agreement with previous *in vivo* studies. However, the maximum reported difference in maximum principal strain was 20% while the maximum principal strain rate differed by only 2% (Al Nazer et al., 2008a). The relatively large error in maximum principal strain may be due to the single bone material property assigned to the tibia. The study by Klodowski *et al.* reduced this inaccuracy of the tibial model by employing CT scans and a more detailed material assignment using the Young's Modulus – density relationship developed by Morgan *et al.* (Morgan, Bayraktar, & Keaveny, 2003). Their results showed that the tibial maximum and minimum principal strains and the maximum shear strain were 512 με, -923 με, and 1444 με, respectively, on the anterior medial aspect of the tibia. This resulted in a

reduction of 16% in the difference between the maximum principal strains for their study compared with previous *in vivo* studies.

Klodowski *et al.* have noticeably improved the methodology proposed by Al Nazer *et al.* by using a more accurate tibial model; however, one of the major limitations present in both of these studies is that the analyses were performed for only a single subject. Currently, there exists very little knowledge of how much bone strain differs among individuals. Such information is important for identifying the critical differences in bone strain among individuals with a high risk of stress fractures and asymptomatic individuals.

1.4 Study Objective

As a step towards understanding critical bone strain under repetitive loading conditions, the purpose of this study was to use the computational approach combining a flexible model of the tibia with a musculoskeletal model in a dynamic simulation to determine a range of expected bone strains during walking for subjects from a homogenous population. The results from this study were compared to previous research using the flexible body approach (Al Nazer et al., 2008a; Klodowski et al., 2009) as well as *in vivo* studies (Burr et al., 1996; Lanyon et al., 1975; C. Milgrom et al., 2000).

CHAPTER 2: METHODS

2.1 Overview

The computation of tibial bone strain during walking is a multistep process. The first step was to create dynamic simulations of walking using subject-specific musculoskeletal models based on previously collected experimental data, including motion trajectories from motion capture, ground reaction forces (GRFs) and electromyography (EMG). Following the creation of the subject-specific musculoskeletal model and walking simulations, the medical imaging data obtained from each subject were used to generate a three-dimensional finite element (FE) representation of the subject's tibia. The medical imaging data were used to generate the geometry of the bone and define the material properties. Once the tibial model was created, an initial modal analysis was performed using token boundary conditions at three landmark locations to generate a modal neutral file. This modal neutral file was imported into the musculoskeletal model for an initial alignment with respect to the subject-specific musculoskeletal model and to determine the muscle attachment sites and joint center locations with respect to the flexible tibia[1]. The ankle and knee joint centers were then used as new boundary conditions to generate a new modal neutral file of the FE tibial model. The modal neutral file is the result of a Craig – Bampton modal analysis that calculates the modal deformation shapes (based on the natural frequencies) for the tibia. This new flexible tibia was then imported into the subject-specific musculoskeletal model prior to the forward dynamic analysis. The last step was to perform a forward dynamic analysis of the walking simulation with the flexible tibia inserted in the

[1] The summation of the deformation modes, used to calculate the strains, for the FE tibial model is called a *flexible tibia* when analyzing bone strain in this study.

musculoskeletal model. With this methodology, the strain values at any location of interest can be computed. This study focused on the bone strain at six locations, including; reference locations at the anterior medial (AM), anterior lateral (AL), lateral (LA), posterior lateral (PL), and posterior medial (PM) aspects of the mid-shaft of the tibia and a simulated staple located distal to the AM location. A general flowchart is shown in Figure 1 below.

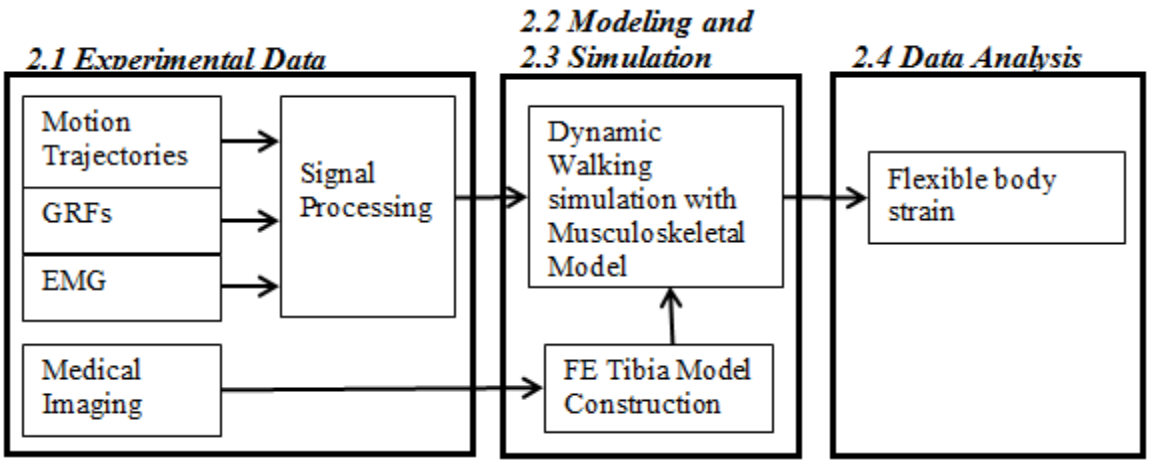

Figure 1: Flowchart for Dynamic Simulations with a Flexible Body

2.2 Experimental Data

2.2.1 Subjects

Experimental and imaging data were collected from 13 male subjects that were part of a larger study conducted at Ball State University. IRB approval for the experimental protocol was obtained, and all experimental data collection was conducted at Ball State University. The inclusion criteria for this study included being a male age 18-27 with no military basic training experience, a body mass index below 28, participating in recreational sport or exercise a minimum of three times per week, being free of musculoskeletal injury, and classified as low risk by ACSM guidelines (Kaminsky, 2006). The subject demographics are outlined in Table 1.

Table 1: Subject Demographics

Number of Subjects	Height (cm)	Mass (kg)	Age (years)
13	180.45+/- 4.6	74.8+/-11.0	20.85+/-1.5

2.2.2 Kinesiological Data

Subjects wearing military combat boots (Altama, Atlanta, GA) were asked to walk at 1.67 m/s for five minutes on an instrumented treadmill (AMTI, Waterton MA). After a warm up period allowing the subjects to acclimate to the treadmill, ten separate motion data sets (five seconds each) were collected during the last minute of the walking trial using a motion capture system with 14 cameras (Vicon, Oxford, UK). Reflective markers were attached according to the lower body Plug-In-Gait marker set (Figure 2) provided by the Vicon system. Reference markers were placed at the hip, knee, ankle, and foot anatomical landmarks, and cluster markers including three (foot) or four (thigh and shank) markers per segment were placed on the left and right thigh, shank and foot, respectively. Marker trajectories were collected at 120 Hz. Surface EMG data were collected using a Bagnoli EMG system (Delsys, Boston, MA), from the vastus medialis (VM), vastus lateralis (VL), tibialis anterior (TA), gastrocnemius (GAS), and soleus (SOL) bilaterally based on the recommendations of Cram *et al.* (Cram, Kasman, and Holtz, 1998). EMG and ground reaction force data were sampled at 2400 Hz.

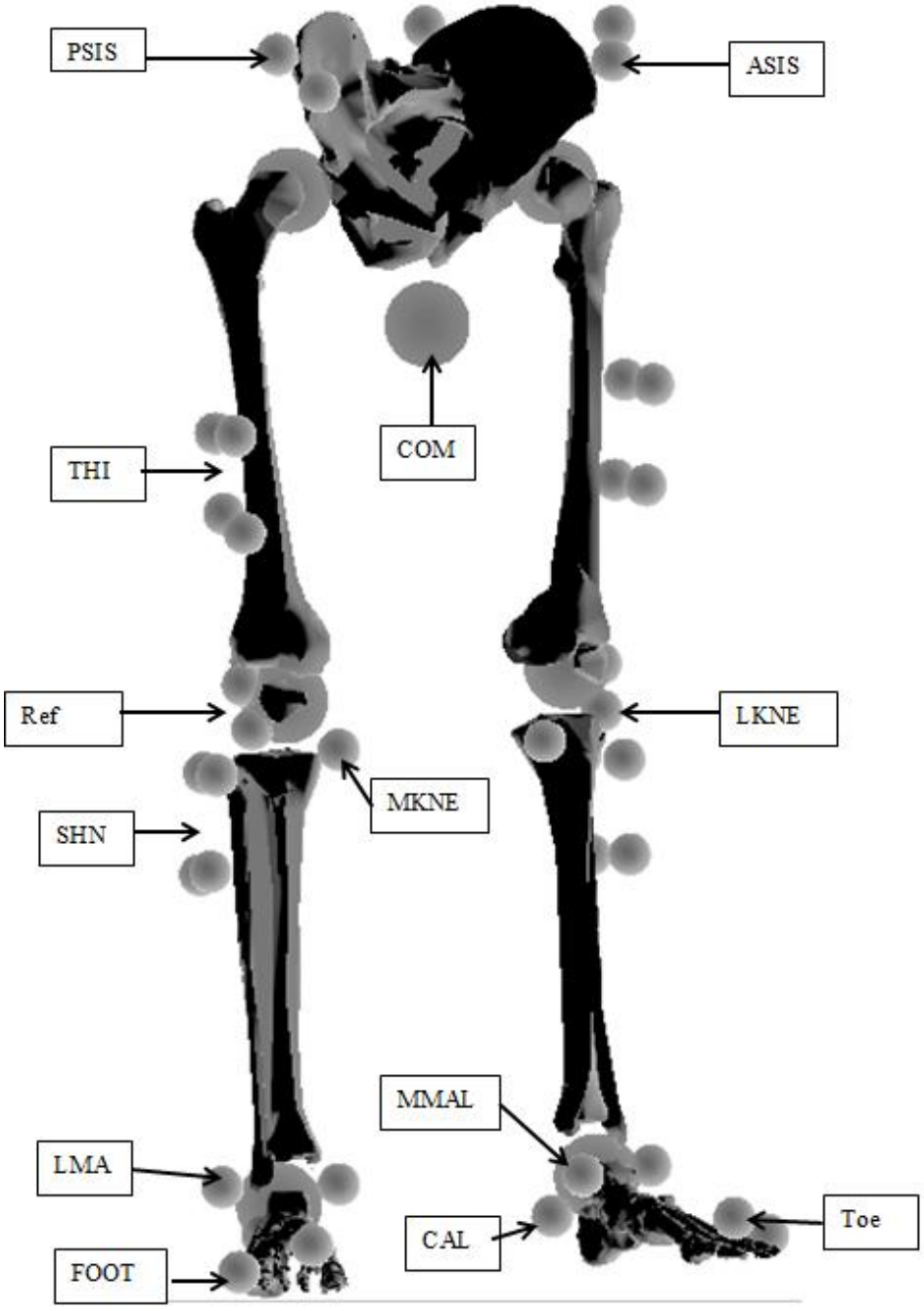

Figure 2: Musculoskeletal Model Setup with Motion Capture Marker Placement and Muscle Locations.

ASIS – Anterior Superior Iliac Spine, PSIS – Posterior Superior Iliac Spine, THI – Thigh cluster, LKNE – lateral side of the knee, MKNE – Medial side of the knee, Ref – Reference node, SHNK – Shank Cluster, LMAL – Lateral Malleolus, MMAL – Medial Malleolus, CALC – Calcaneus, FOOT – foot cluster, COM – Center of Mass location. Marker placement was the same for the right and left limbs.

2.2.3 Medical Imaging Data

Medical imaging data were collected for the length of the tibia using a CT scanner (GE Light Speed VCT General Electric, Fairfeild, CT). The slice thickness was 0.625mm with a 15cm by 15cm field of view and scanning parameters of 120 kVp (peak kilovolts) and 140 mAs (milliampere-second). Images were reconstructed at 512 by 512 pixels.

2.2.4 Signal Processing

The marker trajectories were filtered at 6 Hz using a zero-lag second order recursive low pass filter in Visual 3D (C-motion, Germantown, MA). Force platform data were filtered at 40 Hz using the same filter design. Surface EMG data were rectified and then filtered using a second order low pass Butterworth filter with a cutoff frequency of 10 Hz to generate EMG linear envelopes.

2.3 Modeling

2.3.1 Finite Element Tibia Model Construction

The process for constructing a finite element model of the tibia consisted of three steps. The first was to use the CT scans to create a three dimensional model. This was done by first segmenting the CT scan slices highlighting the cortical bone, trabecular bone, and medullary cavity. The combination of these segments was used to create a 3D representation of the tibial geometry. The second step was to create a mesh that was used in the finite element analysis (or modal analysis). The final step was to assign a material property scheme. Based on the recommendations of Gray *et al.*, a total of 600 regions of material properties were applied to the FE tibial model, with 300 for the cortical region of bone and 300 for the cavity and trabecular regions (Gray et al., 2008). The Young's Modulus assigned to each of the 600 regions was calculated using the density of the tibia (represented by Hounsfield Units in a CT scan). A

Hounsfield Unit (HU) represents the density of an object with respect to water (HU of water is zero). A flowchart for the creation of the FE tibial model is shown in Figure 3.

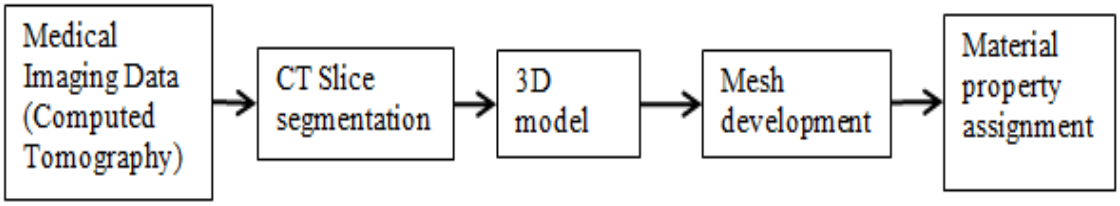

Figure 3: FE Tibial Model Creation Flowchart

2.3.2 CT Slice Segmentation and Model Creation

Due to the lower intensity used in the CT scans (120 kVp compared to a typical intensity of 160 kVp), which result in lower HU values for the CT pixels, the common HU threshold values for cortical (662 – 1986 HU) and trabecular bone (148-661 HU) cannot be used for this study. Therefore, an intensity thresholding technique similar to one validated by Rathnayaka *et al.* (Rathnayaka et al., 2010) was used to determine the threshold values for each region of bone (cortical, trabecular, and cavity). By creating a pathline crossing a single slice from the CT scans generated in Mimics 14.0 (Materialise, Leuven Belgium) a graph of the HU intensity range seen in the middle third of the tibia can be created. Using this graph, three distinct thresholds for the cavity, cortical, and trabecular bone can be selected for the tibia. An example of the pathline and pathline graph can be seen in Figures 4 and 5 below.

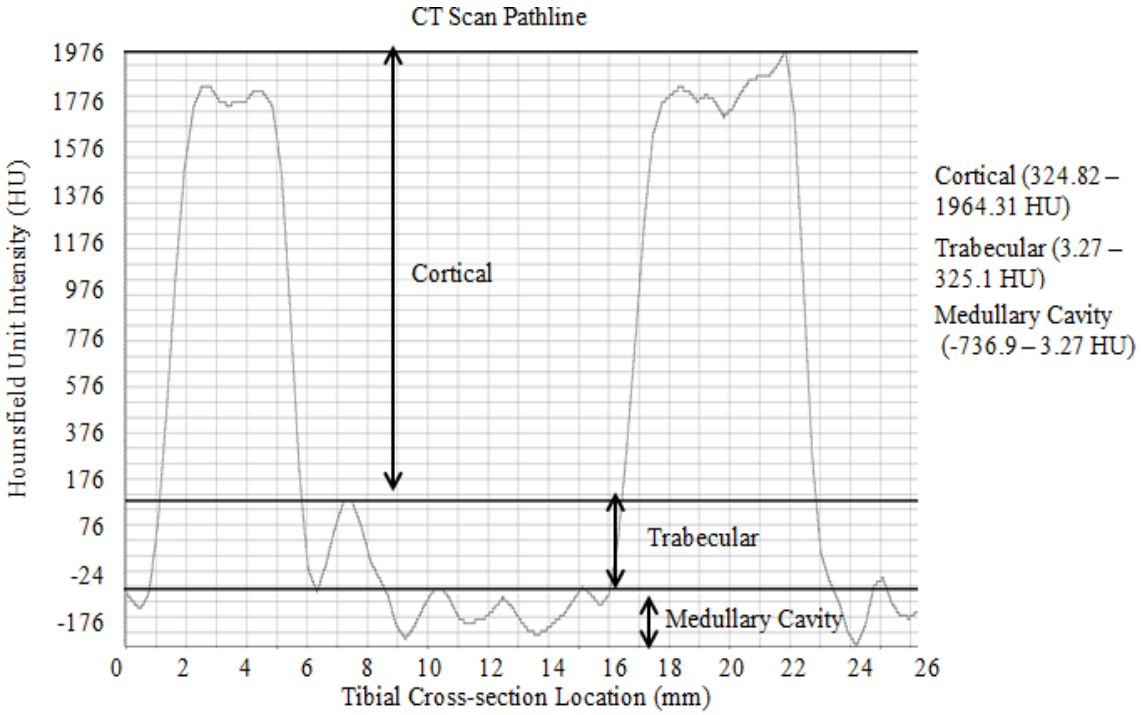

Figure 4: Graph Showing the Threshold Regions for Cortical Bone, Trabecular Bone, and the Medullary Cavity

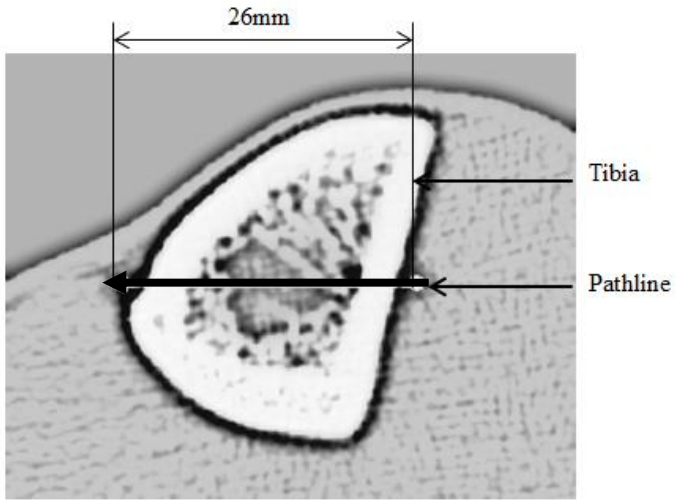

Figure 5: Cross-Sectional Area with a Pathline of a Representative Tibia

The layers in Figure 4 (above) mark the threshold intensity ranges of the cortical bone, trabecular bone, and medullary cavity segments. The HU value limits reported in Figure 4 are the mean limits taken from all subjects. Using these thresholds and some manual masking near the proximal and distal ends of the tibia, a 3D solid model of the tibia was created for further analysis.

2.3.3 Mesh Development

The 3D model was exported to 3-Matic 5.1 (Materialise, Leuven, Belgium) where a surface mesh was automatically generated. The surface mesh provides a boundary for the automatic formulation of a solid mesh. The surface mesh created in 3-Matic was then exported to MD MARC (MSC.Software, Santa Ana, CA) and a solid mesh using hexahedral elements with a target element edge length of 3mm was generated. This level of refinement was chosen due to the complexity of the bone geometry and computational limitations.

2.3.4 Material Property Assignment

Once the 3D tibial model was created and meshed, the material properties (Young's Modulus and Poisson's Ratio) were applied. The CT images were broken down into rectangular 3D elements (with a thickness that is half the width and length) called voxels. The HU, determined in the segmentation process, was applied to each voxel. To provide a calibration scale for determining the bone apparent density, a phantom with known material densities was scanned with the same CT scan parameters used for the subjects' bone scanning. A model of the phantom and the material densities used for calibration are shown in Figure 6 and Table 2, respectively.

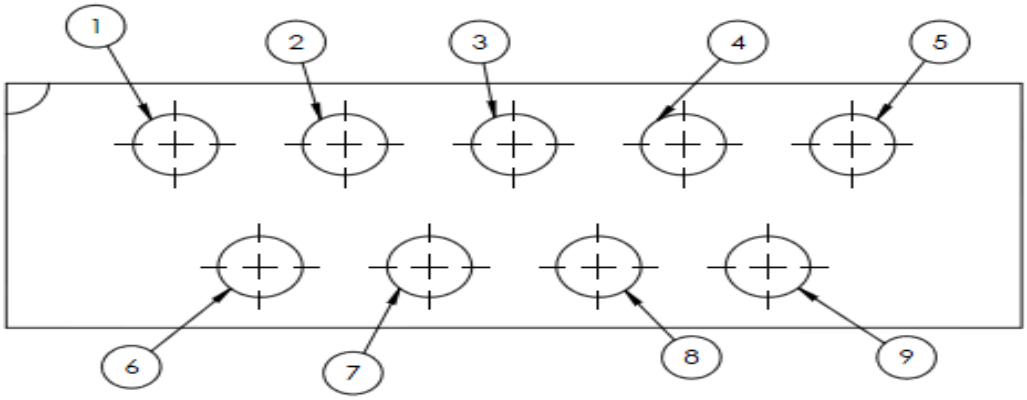

Figure 6: Model of the Phantom Used for Density Calibration

Table 2: Phantom Calibration Material Densities

	Material	Bulk Density
1	Empty	N/A
2	UHMW – Ultrahigh Molecular Weight Polyethylene	0.93 g/cm^3
3	ABS – Acrylonitrile Butadiene Styrene	1.02 g/cm^3
4	Nylon	1.13 g/cm^3
5	PEEK – Polyether Ether Ketone	1.3 g/cm^3
6	Acetal	1.42 g/cm^3
7	PET – Polyethylene Terephthalate	1.44 g/cm^3
8	FR4 – Glass	1.86 g/cm^3
9	Virgin PTFE – Polytetraflouroethylene	2.18 g/cm^3

Using the values in Table 2 and the HU values obtained from the CT scan of the phantom, a relationship between density and HU was obtained. The density values, once computed, were used to calculate Young's Modulus using the following established power law relationships for cortical bone and trabecular bone (Linde, Hvid, & Madsen, 1992; Snyder & Schneider, 1991).

$$E = 3.891 * \rho_{app}^{2.39} \text{ (Cortical Bone)} \quad 2.1$$

$$E = 4.778 * \rho_{app}^{1.99} \text{ (Trabecular Bone)} \quad 2.2$$

Where ρ_{app} is the apparent density in grams per cubic centimeter (g/cm^3) and E is Young's Modulus in Giga Pascals (GPa). As shown by Gray *et al.*, the number of material property groups assigned to the tibia model can influence the strain results (Gray et al., 2008). Gray *et al.* found that the strain results (strain energy, displacement, and maximum principal strain) could be accurately estimated using 600 material property groups (Gray et al., 2008). Based on these results, 300 material properties were applied to all the elements in the cortical bone region, and 300 material properties were applied to all the elements in the trabecular bone region and the medullary cavity.

2.4 Dynamic Simulation of Walking

The dynamic simulations of walking were generated using musculoskeletal modeling and simulation software (LifeMOD, LifeModeler, San Clemente, CA). The simulations were created in two steps: 1) performing an inverse kinematics analysis using the experimental marker trajectories and a subject-specific musculoskeletal model, and 2) performing a forward dynamics simulation using the experimental ground reaction force (GRF) data, simulated joint torques, and simulated muscle excitations.

2.4.1 Subject-Specific Musculoskeletal Model

A subject-specific three dimensional musculoskeletal model, based on the individual subject's height, mass, age, and sex, that consisted of seven rigid body segments for the lower body (a pelvis, two femurs, two tibias, and two feet) was created using the GeBOD program (Cheng, Obergefell, & Rizer, 1996). This model was scaled using joint center calculations from Visual 3D (C-Motion, Germantown, MA). The hip joints were modeled as ball and socket joints, while the knee and ankle joints were modeled as simple hinge joints.

The initial posture was set by matching the expected locations of the markers on the model with the experimental marker locations (Plug-In-Gait, Vicon) from the first frame of the static motion capture trial. The cluster markers from this frame were then added to their respective segments in the model. This method for setting the posture resulted in the model being aligned with the first frame of the static motion trial and the cluster markers being attached at the same location as defined in Visual 3D.

2.4.2 Gait Simulation

The kinematics (joint angles and muscle lengths with respect to time) of each walking trial were calculated using the experimental marker trajectories in an inverse kinematics (IK)

analysis. The initial posture was set by synchronizing the previously created model markers with the first frame of the motion trajectory data. The joint angles and muscle lengths computed during the IK analysis were used as inputs to the subsequent forward dynamics simulation. The forward dynamics simulation was driven using PD-controlled joint actuators, for the left and right hip, and the left knee and ankle joints, and PID-controlled muscle actuators for the right lower limb. The joint torques and muscle forces generated by these actuators depended on the joint angles and muscle lengths obtained in the IK analysis. The joint torques were modeled as simple PD controlled servomotors, and the muscle forces were defined by the following equations.

$$F = P_{gain}(P_{error}) + I_{gain}(I_{error}) + D_{gain}(D_{error}) \quad 2.3$$

where

$$P_{error} = \frac{(Target\ Value - Current\ Value)}{(ROM)} \quad 2.4$$

$$D_{error} = first\ derivative\ of\ P_{error} \quad 2.5$$

$$I_{error} = \int P_{error}\, dt \quad 2.6$$

For Equations 2.3 through 2.6, P_{gain} is the proportional gain, I_{gain} is the integral gain, and D_{gain} is the derivative gain. For the PD-controlled joint torque actuators, Equation 2.3 above loses the I_{gain} (I_{error}) term. The target value was the target length of the muscle, or joint angle calculated during the IK analysis, the current value was the value at the current time step in the forward dynamics simulation, and ROM is the range of motion of the muscle (the difference between the shortest and longest lengths experienced by the muscle), or the joint. The P, I, and D terms for the muscles, and the P and D terms for the joints are shown in Table 3 below.

Table 3: PID Values for the Model Muscles and Joints

	Muscles	Joints
P	1×10^7	2.87×10^5
I	1×10^6	-
D	1×10^4	2.87×10^3

There were 15 muscles present in the forward dynamics simulation, including the biceps femoris short head, vastus medialis, vastus intermedius, vastus lateralis, gastrocnemius, soleus, tibialis posterior, flexor digitorum, flexor hallucis, tibialis anterior, peroneus brevis, peroneus longus, peroneus tertius, extensor digitorum, and extensor hallucis. Prior to the forward dynamics analysis, the flexible tibia (Figure 8) was integrated into the subject-specific musculoskeletal model, replacing the original tibia in the model. The forward dynamics simulation was generated such that all leg joint angles determined in the IK analysis were tracked by activating the PD-controlled joint and PID-controlled muscle actuators with applied experimental GRFs at the center of pressure of the feet. The motion of the center of mass of the pelvis was prescribed to follow the pelvis kinematics determined during the IK analysis. The dynamic equations of motion for the forward dynamics simulation were integrated with a time step of 0.01, and the default integrator tolerance (maximum error of 0.001) defined in LifeMOD.

2.4.3 Flexible Tibia Incorporation

Due to the highly complex geometry of the tibia, finite element (FE) models have very high nodal degrees of freedom. Since the computational expense of performing a dynamic analysis on such a complex model is extremely high, a modal analysis was performed on the FE tibia to create a flexible model of the tibia (a flexible tibia) to be imported into the subject-specific musculoskeletal model. An initial Craig – Bampton modal analysis was performed using token boundary conditions to generate a flexible tibia that was used to align the flexible tibia with the subject-specific musculoskeletal model. The nodes in the FE tibia model corresponding to the

tibial landmarks in the motion trajectory data were manually selected for aligning the flexible tibia with the rest of the musculoskeletal model. The alignment of the flexible tibia was accomplished by matching the selected nodes with the corresponding tibial landmarks in the rigid model, such that the flexible tibia was fitted in the space between the knee and ankle joints, with the long axis of the tibia being in line with the knee and ankle joint centers. After aligning the flexible tibia in the musculoskeletal model, the muscle attachment points, and knee and ankle joint center locations were calculated and exported from LifeMOD. A second Craig – Bampton modal analysis was performed using boundary conditions applied at the knee and ankle joint centers, respectively. The new flexible tibia was used during the forward dynamics simulation to calculate the tibial strain during walking. A flowchart of the steps involved in integrating the flexible body into the musculoskeletal model is shown in Figure 7 below.

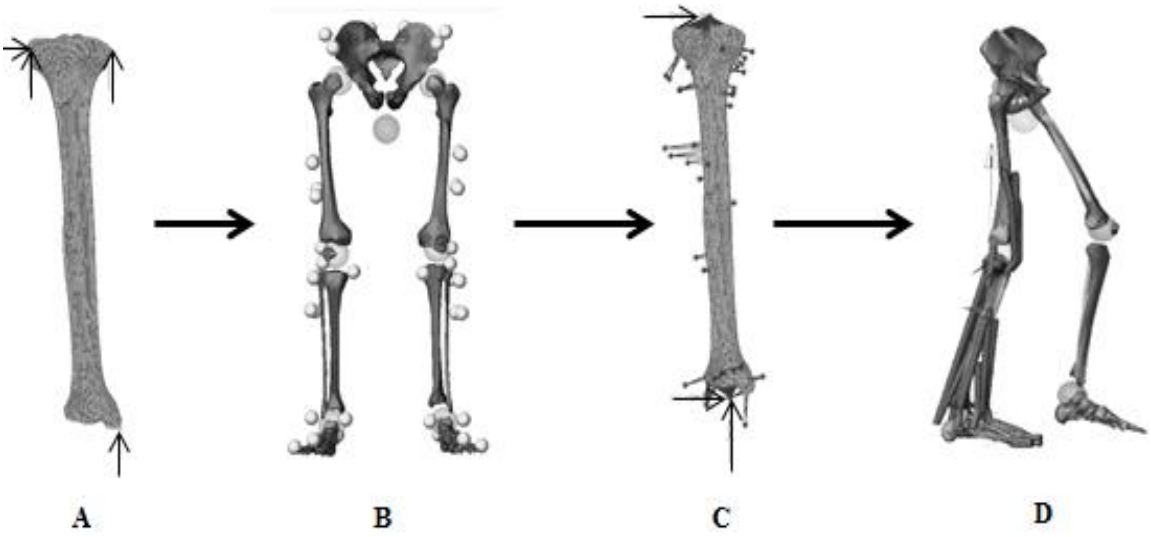

Figure 7: Flowchart for Incorporating a Flexible Tibia into a Musculoskeletal Model. A) Flexible tibia with token BCs. B) Alignment of the flexible tibia with the musculoskeletal model. C) Rebuild the flexible tibia with BCs at the knee and ankle. D) Insert the new flexible tibia into the dynamic simulation for strain calculations

In the original rigid musculoskeletal model, the muscle attachment sites were defined using a single point on the rigid body segments. The use of point attachments is reasonable for a rigid body; however, they will cause unrealistically high strains in a flexible body. In order to fix

this problem, nodes at the locations of the muscle attachment sites (exported from LifeMOD during the initial alignment of the flexible tibia) were connected to the six nearest nodes on the flexible tibia by rigid body elements (RBEs), alleviating the point load of a single node attachment site. The six nodes represent an approximation of the physiological insertion area for each respective muscle. The RBEs connecting the muscle attachment sites to the flexible body were set to represent a rigid fixation of the muscle to the bone. RBEs were also used to represent the joint contacts for the knee and ankle, respectively, by connecting a node at the knee and ankle joint centers to the corresponding joint surfaces (approximated as flat surfaces). A detailed representation of the muscle attachment sites and joint centers is shown in Figure 8.

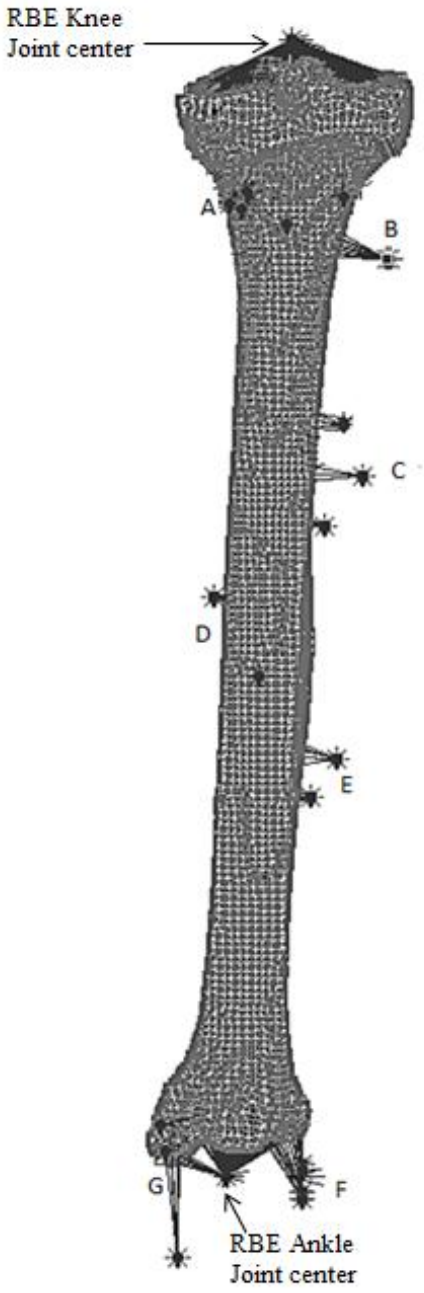

Figure 8: Flexible Tibia with RBEs for Muscle Attachment Sites and Joint Centers.

Muscle Attachments for groups (A) medial gastrocnemius(B) lateral gastrocnemius, biceps femoris short head, (C) peroneus longus (1st attachment), extensor digitorum, extensor hallucis, (D) flexor digitorum(1st attachment), flexor hallucis (1st attachment), (E) peroneus brevis (1st attachment), peroneus tertius, (F) peroneus brevis (2nd and 3rd attachments), peroneus longus (2nd and 3rd attachments), (G) tibialis posterior (2nd attachment) flexor digitorum (2nd attachment), and flexor hallucis (2nd attachment). Not shown are the vastus medialis, vastus intermedius, vastus lateralis, tibialis anterior, and soleus attachment sites

In order to compare the bone strain results between subjects and with previous research using a similar computational approach, surface nodes were selected in groups of four at five reference locations around the mid-shaft of the FE tibia (Figure 9 – A). In addition to these reference locations, a simulated staple consisting of eight nodes was selected on the anterior medial aspect and distal to the mid-shaft of the tibia (Figure 9 – B) in order to compare with previous *in vivo* studies.

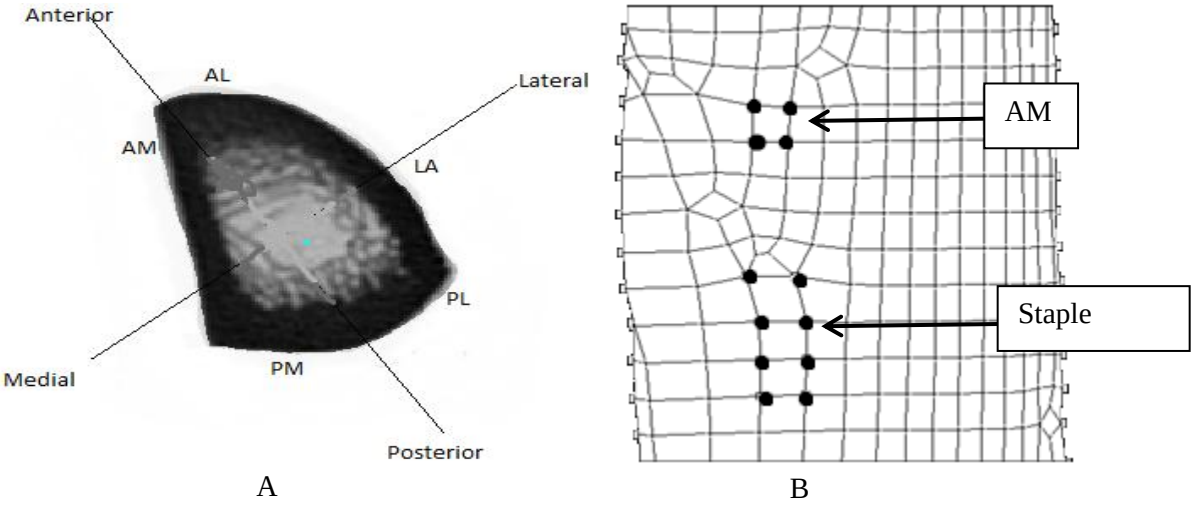

Figure 9: Strain Locations
A) Shows the five mid-shaft positions, AL - Anterior Lateral, AM - Anterior Medial, LA - Lateral, PL - Posterior Lateral, PM - Posterior Medial. B) Showing a frontal view of the 4 nodes at AM (similar pattern at other 4 locations), and the position of the simulated staple.

2.5 Data Analysis

2.5.1 Strain Data

Strain data during walking were computed using the Durability Plug-in for ADAMS/View (MSC.Software, Santa Anna, CA) that was incorporated in the LifeMOD analysis framework. Maximum principal, minimum principal, and maximum shear strain data were obtained from the four nodes at the reference locations on the flexible tibia model and filtered using a second order low pass Butterworth filter with a seven Hz cutoff frequency (Turner, Yoshikawa, Forwood, Sun, & Burr, 1995). The filtered data was then scaled to microstrain and

time-normalized to a single gait cycle (from right heel strike to the subsequent ipsi-lateral heel strike). Due to the noise included in the ground reaction force data, the right foot's heel strike was determined by finding the time in the simulation of walking on the treadmill when the anterior-posterior (A/P) position of the right foot's center of mass was at a maximum, while toe off was considered to be the time when the A/P position of the right foot's center of mass was at a minimum. The mean strain calculated from the eight nodes of the simulated staple, or four nodes for each reference location, was used as a representation of the strain value for each location, respectively. The strain rates were calculated by differentiating the filtered and scaled (microstrain) data. Strain data were computed for subjects with a minimum of 12 complete strides. A complete stride was defined as any stride following the first stride with a complete gait cycle. The first stride was excluded due to the unknown initial positioning of the right foot.

2.5.2 Model Validation

For the purpose of validating the dynamic walking simulation, joint angles, joint torques, and muscle excitation patterns were compared between the forward dynamics simulation, including the flexible tibia, and the experimental data. The comparison between experimental EMG and muscle excitation patterns from the simulation was performed by first determining whether the difference in activation timing was significantly different by finding the 95% confidence interval for the coefficient of cross correlation (Li & Caldwell, 1999), and then determining whether the cross correlation coefficient for the two excitations was within that range. The joint angles and joint torques for the forward dynamics simulation and the experimental joint angles and joint torques were similarly compared using the 95% confidence interval of the coefficient of cross correlation. The cross correlation coefficient r_{xy} is the maximum value of

$$r_{xy} = \frac{c_{xy}(k)}{\sqrt{c_{xx}(0)c_{yy}(0)}} \quad 2.7$$

where $c_{xy}(k)$ is defined as

$$c_{xy}(k) = \begin{cases} \sum_{t=1}^{N-k}(x_t - \bar{x})(y_{t+k} - \bar{y}) + \sum_{t=N-k+1}^{N}(x_t - \bar{x})(y_{t-N+k} - \bar{y}) \text{ When k} = 1,2,\ldots,N \\ \sum_{t=1}^{N}(x_t - \bar{x})(y_t - \bar{y}) \text{ When k} = 0 \end{cases} \quad 2.8$$

and c_{xx} and c_{yy} are defined as

$$c_{xx} = \sum_{t=1}^{N}(x_t - \bar{x})^2$$
$$c_{yy} = \sum_{t=1}^{N}(y_t - \bar{y})^2 \quad 2.9$$

For the above equations, k is a number indicating a time shift of one signal with respect to the other (k = 0 for two signals synchronized in time), N is the number of data points in the time series, x_t is the value of the first signal at time t, and $\bar{x}$ is the average of the first signal, y_t is the value of the second signal at time t, and $\bar{y}$ is the average of the second signal. The 95% confidence interval for r_{xy} is determined by the lower and upper confidence interval bounds

$$\left(\frac{e^{2h_1}-1}{e^{2h_1}+1}, \frac{e^{2h_2}-1}{e^{2h_2}+1}\right) \quad 2.10$$

where

$$h_1 = \frac{1}{2} * \ln\frac{1+r_{xy}}{1+r_{xy}} - \frac{1.96}{\sqrt{N-3}} \quad 2.11$$

and

$$h_2 = \frac{1}{2} * \ln \frac{1+r_{xy}}{1+r_{xy}} + \frac{1.96}{\sqrt{N-3}} \quad 2.12$$

2.5.3 Statistical Analysis

The strain curves from each subject (12 strides) were averaged, assuming that the mean curve could represent the subject's strain patterns. This assumption was evaluated for each subject by computing the Coefficient of Multiple Correlation (CMC) at each location of strain measurement. The calculation of CMC was based on the method used by Kadaba *et al.* (Kadaba et al., 1989). The CMC was calculated using the following equations, where CMC is equal to the positive square root of R^2.

$$R^2 = 1 - \frac{\sum_{i=1}^{M}\sum_{j=1}^{N}\sum_{k=1}^{T}\left(Y_{ijk}-\bar{Y}_{ik}\right)^2/[M*T*(N-1)]}{\sum_{i=1}^{M}\sum_{j=1}^{N}\sum_{k=1}^{T}\left(Y_{ijk}-\bar{Y}_{i}\right)^2/[M*(N*T-1)]} \quad 2.13$$

$$\bar{Y}_{ik} = \frac{1}{N}\sum_{j=1}^{N} Y_{ijk} \quad 2.14$$

$$\bar{Y}_{i} = \frac{1}{N*T}\sum_{j=1}^{N}\sum_{k=1}^{T} Y_{ijk} \quad 2.15$$

For the above equations, M represents the number of locations (three strains multiplied by six locations), N represents the number of strides, and T represents the time (normalized to 100 points). Y_{ik} represents the average value at time k, where $1 \leq k \leq 101$, for the *ith* location. Y_i represents the "grand" mean for the *ith* location.

To establish the normative range of strain data for the population represented by the subjects in this study, the mean strains from the subjects were bootstrapped to generate a larger sample dataset. The bootstrap method is a statistical resampling technique used when the distribution of the original population is unknown (TC, 1998). In this study, 1000 indexes generated by randomly selecting a value between 1 and 12 (representing each subject) were used

to generate 1000 strain curves based on the original twelve. Due to the random nature of selecting the indices, the subjects were not guaranteed to be selected an equal number of times. The mean, standard deviation, and 2.5 and 97.5 percentile bounds of this dataset were then calculated. The ranges covering the normal population were calculated using the upper (97.5 percentile) and lower (2.5 percentile) values calculated at each normalized time step (1 to 101). These ranges were plotted against the percentage of the gait cycle to show the expected range of the strain profile during walking. The strain rate data was treated in the same manner, creating expected ranges for the strain rates at each location.

A comparison of the selection of the low pass filter's cutoff frequency was performed to determine if there was a statistical difference in choosing frequencies of 3, 5, or 16.04 Hz, instead of 7 Hz. The 95% confidence interval of the mean strain of a bootstrapped dataset was calculated for each frequency choice. A statistical difference was considered to exist when the confidence intervals of the mean strains were not overlapping.

CHAPTER 3: RESULTS

3.1 Model Validation

3.1.1 Kinematic, Kinetic, and Muscle Activation Comparison

The coefficient of cross correlation showed that there were no significant differences between the subjects' experimental joint angles and the simulated joint angles (mean r_{xy}: 0.95, 0.93, and 0.92 for the ankle, knee and hip) or torques (mean r_{xy}: 0.98, 0.82, 0.92 for the ankle, knee and hip), or between the simulated muscle excitation timing and the experimental EMG timing (mean r_{xy}: 0.62, 0.75, 0.57, 0.62, 0.59 for the gastrocnemius, soleus, tibialis anterior, vastus lateralis, and vastus medialis, respectively). A significant difference was considered to exist if the r_{xy} values fell outside of the 95% confidence interval calculated in Equation 2.10. The results from this analysis are shown in Table 4 below. The average root-mean-square-errors for the hip, knee, and ankle angles were 7.77˚, 9.38˚, and 2.85˚, respectively. A comparison of the experimental and simulated joint angles and torques plus or minus one standard deviation are shown in Figure 10 and Figure 11, respectively.

In order to calculate the necessary joint torques for the PID controlled joints (left and right hip, left knee, and left ankle), the forward dynamics simulation required a ground reaction force (GRF) input. The GRF inputs used for this simulation were the experimental GRFs collected during the original walking trials. A plot of the mean vertical (Z), anterior-posterior (Y), and medial-lateral (X) ground reaction forces plus and minus one standard deviation is shown in Figure A-1 of Appendix A.

Table 4: Confidence Intervals for r_{xy} Values from the Kinematic, Kinetic, and EMG Comparisons

		Lower CI	r_{xy}	Upper CI
Kinematic Comparison	Ankle	0.9227	0.9468	0.9636
	Knee	0.9011	0.9284	0.9491
	Hip	0.8737	0.9123	0.9397
Kinetic Comparison	Ankle	0.9741	0.9825	0.9882
	Knee	0.7398	0.8164	0.8723
	Hip	0.8825	0.9191	0.9447
Muscle Activation Comparison	Gastrocnemius	0.4796	0.6156	0.723
	Soleus	0.6548	0.753	0.8263
	Tibialis Anterior	0.4206	0.568	0.6864
	Vastus Lateralis	0.482	0.6179	0.7249
	vastus Medialis	0.453	0.5946	0.7071

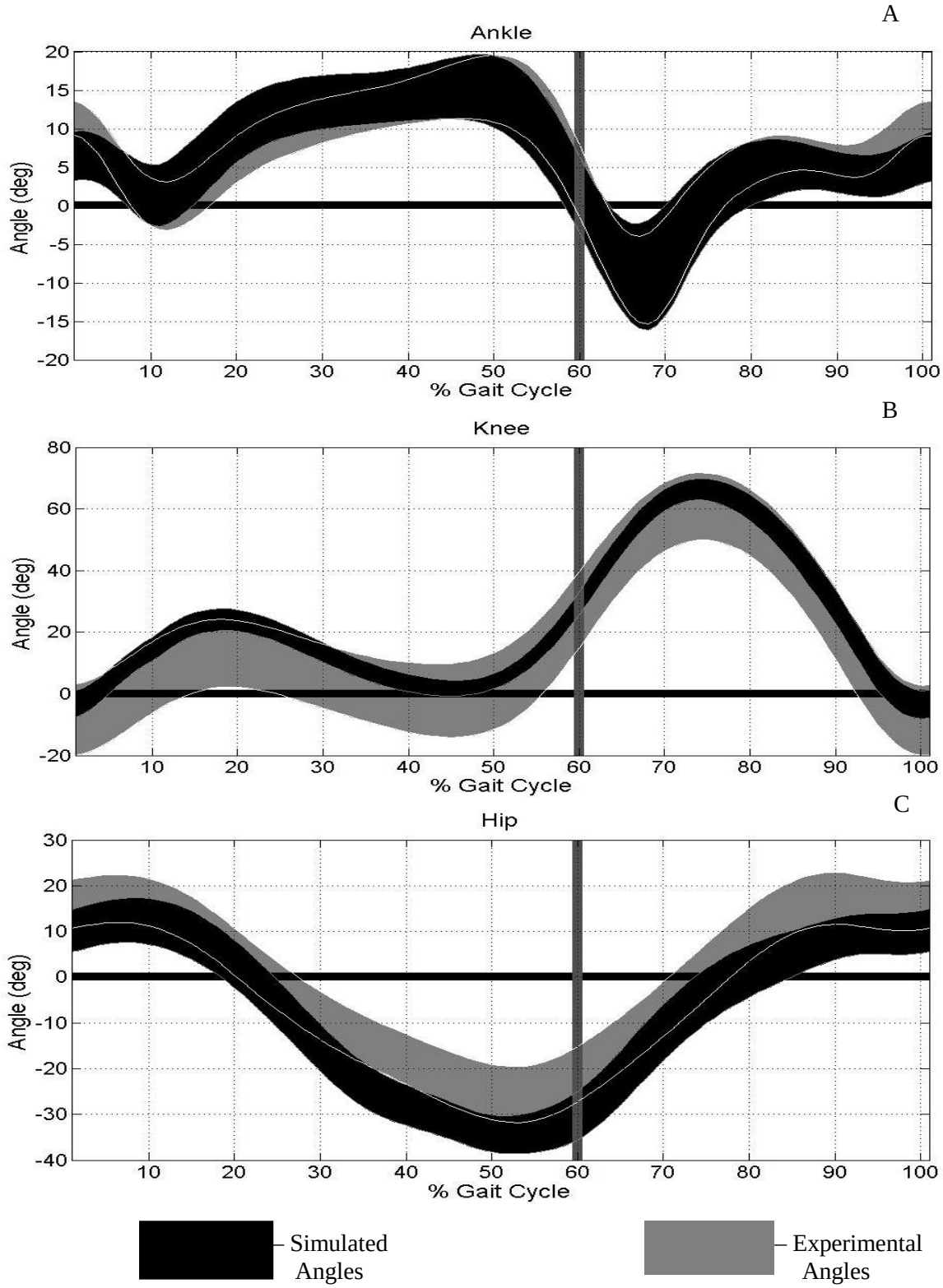

Figure 10: Joint Angle Comparisons for the (A) Ankle, (B) Knee, and (C) Hip. The vertical bands indicate the typical timing of toe-off.

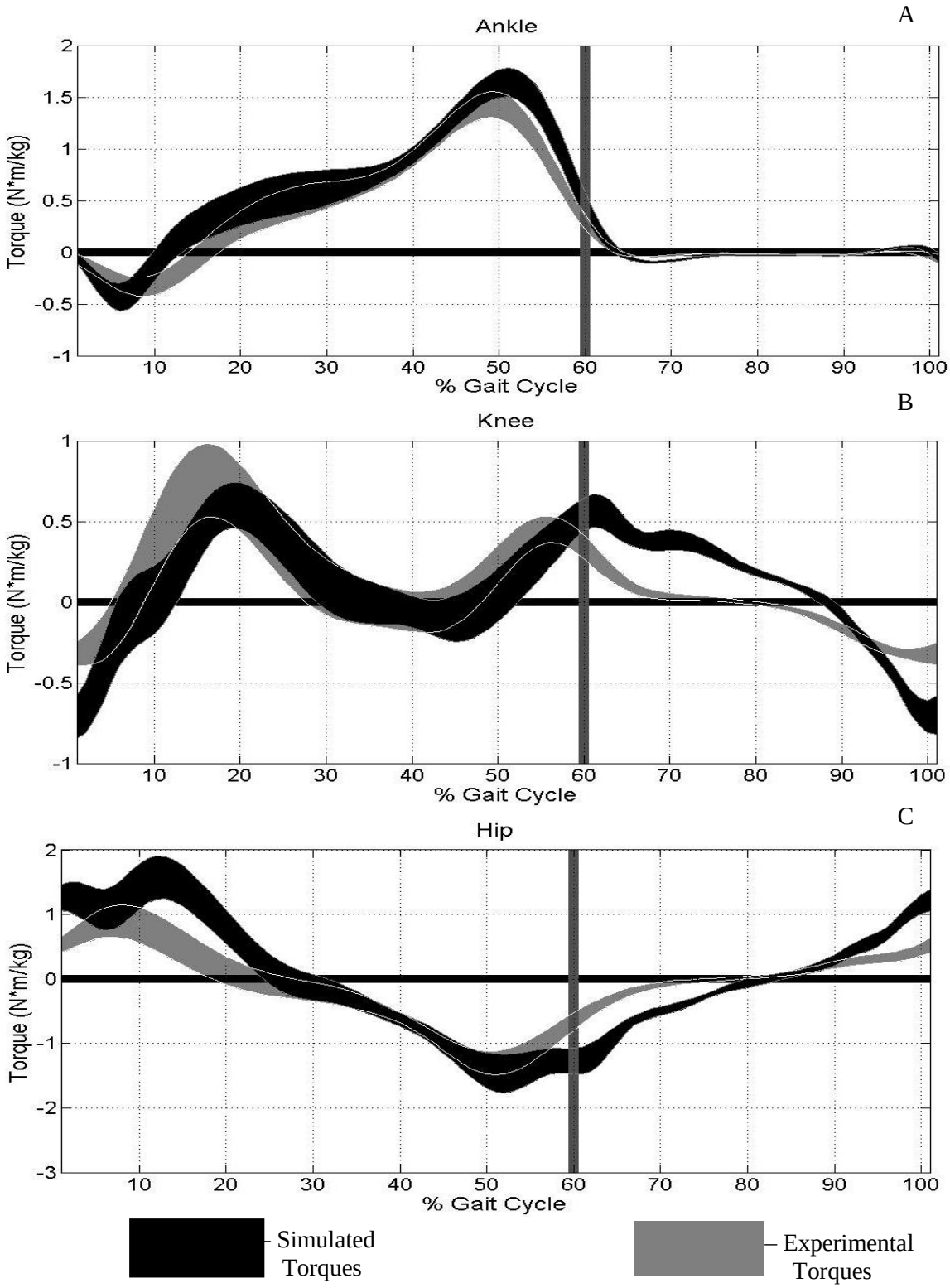

Figure 11: Joint Torque Comparisons for the (A) Ankle, (B) Knee, and (C) Hip. The vertical bands indicate the typical timing of toe-off.

A representative plot of the experimental EMG and simulated muscle excitation patterns is shown in Figure 12. The EMG data and simulated muscle excitations for each muscle were normalized to the maximum value per stride.

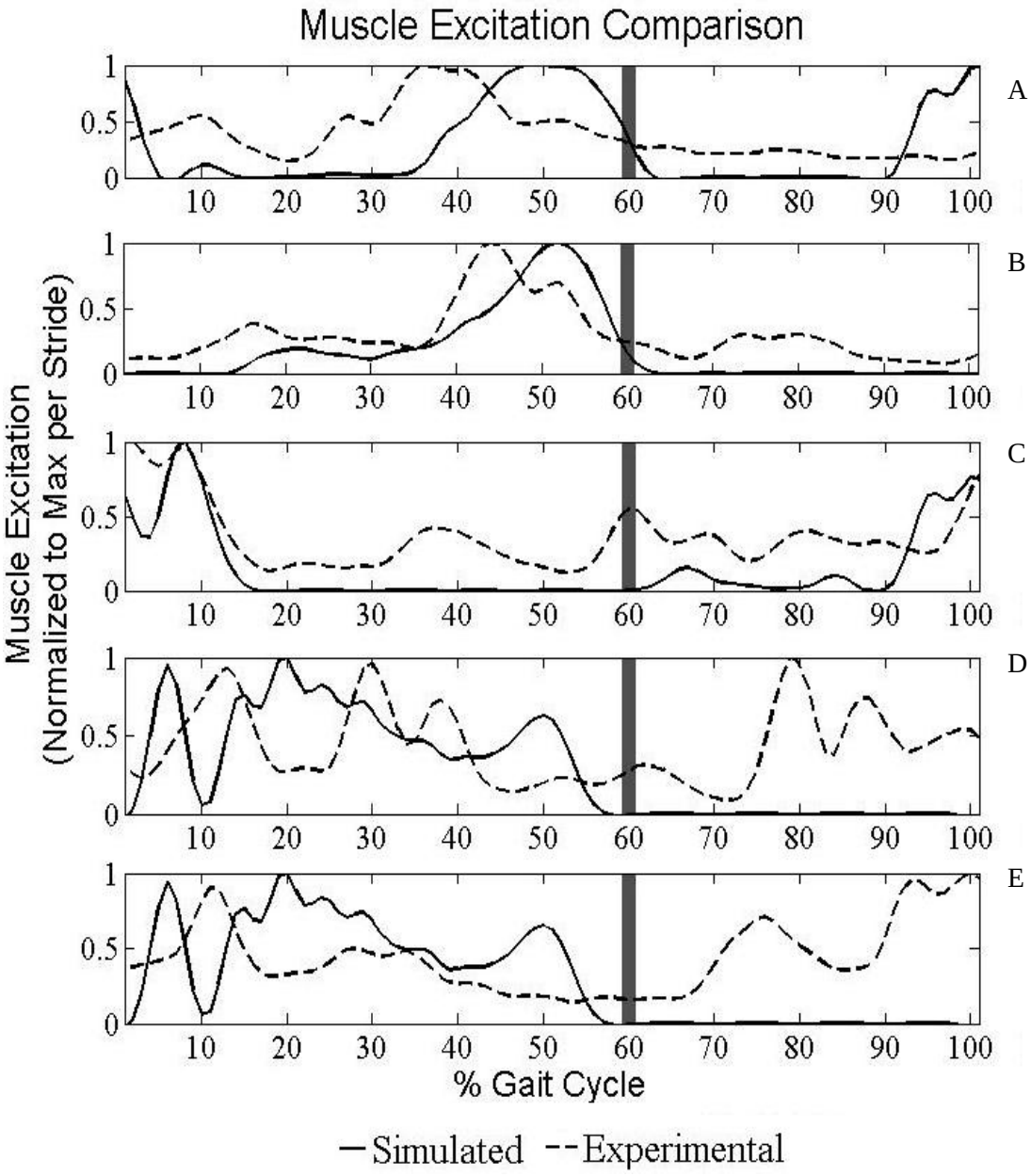

Figure 12: Experimental EMG and Simulated Muscle Excitation Comparison.

(A) Gastrocnemius, (B) Soleus, (C) Tibialis Anterior, (D) Vastus Lateralis, and (E) Vastus Medialis. The vertical bands indicate time of toe-off for the subject. Curves shown were filtered using a second order low pass Butterworth filter with a cutoff frequency of 10 Hz.

3.2 Peak Strain and Strain Rate

3.2.1 Comparison with Previous Research

The results obtained from integrating a flexible tibia into a dynamic simulation of walking were compared with previous *in vivo* studies (Burr et al., 1996; Lanyon et al., 1975; C. Milgrom et al., 2000) and previous studies using similar methodologies to calculate bone strain computationally (Al Nazer et al., 2008a; Klodowski et al., 2009). The anterior medial location was a common location between this study and previous computational models while the simulated staple was a common site between this study and previous *in vivo* studies. The results from previous computational models and *in vivo* studies are shown in Table 5 along with the present study's results.

Table 5: Strain and Strain Rate Comparison with Previous Research (maximum values)

		Peak Strain (με)			Peak Strain Rate (με/sec)		
Study	Result Type	Max Principal	Min Principal	Max Shear	Max Principal	Min Principal	Max Shear
Anterior Medial Location[1]	**Simulation**	**488**	**-473**	**814**	**6946**	**-3588**	**8612**
Simulated Staple[1]	**Simulation**	**543**	**-453**	**838**	**7921**	**-3494**	**10390**
Klodowski *et al.* (2009)	Simulation	512	-932	1444	[2]	[2]	[2]
Al Nazer *et al.* (2008a)	Simulation	305	-645	948	4000	-7000	10000
Milgrom *et al.* (2000)	Experimental	500	-250	980	3200	-1900	4500
Burr *et al.*(1996)	Experimental	437	-544	871	11006	-7183	16162
Lanyon *et al.* (1975)	Experimental	311	-368	[2]	[2]	-3370	[2]

1 - Values from the present study
2 - Indicates a value that was not reported in the literature

The study by Lanyon *et al.* was the first use of strain gauges *in vivo* to measure bone strain during a dynamic activity, and has become the standard of comparison for later research

(Lanyon et al., 1975). The values for the maximum and minimum principal strains in the present study were 42% and 18% higher than the results shown by Lanyon *et al.* (Lanyon et al., 1975). Other prominent studies for *in vivo* bone strain of the tibia include studies performed by Burr *et al.* and Milgrom *et al.* (Burr et al., 1996; C. Milgrom et al., 2000). The maximum principal strain calculated in this study was 19% higher than the results obtained by Burr *et al.*, while the minimum principal strain was 17% lower, and the maximum shear strain was 3% lower (Burr et al., 1996). The maximum principal, minimum principal, and maximum shear strains in this study were 8% higher, 45% higher, and 17% lower than the results reported by Milgrom *et al.* (C. Milgrom et al., 2000). Compared to Lanyon *et al.*, the calculated minimum principal strain rate was 3% higher (Lanyon et al., 1975). The maximum principal strain rate for this study was 28% lower than Burr *et al.*'s results, while the minimum principal strain rate was 51% lower, and the maximum shear strain rate was 35% lower (Burr et al., 1996). The maximum principal strain varied by 59% (higher), while the minimum principal was 46% higher, and the maximum shear strain was 57% higher than the results reported by Milgrom *et al.* (C. Milgrom et al., 2000).

The results reported by Al Nazer *et al.* and Klodowski *et al.* showed similar differences to the differences from *in vivo* data (Al Nazer et al., 2008a; Klodowski et al., 2009). The maximum principal strain from this study was 5% lower than that reported by Klodowski *et al.*, while the maximum shear strain was 44% lower (1444με compared to814με), and the minimum principal strain was 49% lower (-932με and -473με) (Klodowski et al., 2009). The study by Al Nazer *et al.* reported lower values overall, with a maximum principal strain of 305με (37% lower), a maximum shear strain of 948με (14% higher), and a minimum principal strain of -645με (27% higher) (Al Nazer et al., 2008a). The maximum principal, minimum principal, and maximum shear strain rates for this study were 22% higher, 62% lower, and 32% lower than the results reported by Al Nazer *et al.* (Al Nazer et al., 2008a).

3.2.2 Strain and Strain Rate Variability

Strain and strain rate data were obtained from five reference locations spaced around the tibia at mid-shaft as well as a simulated staple located distal of mid-shaft on the anterior medial (AM) face of the tibia (see Figure 9 in Chapter 2). The inter-subject mean and standard deviation for peak maximum principal, minimum principal and maximum shear strains and strain rates over a gait cycle are shown in Table 6. The simulated staple and the anterior-medial reference nodes showed very similar strain and strain rate profiles due to their nearness.

Table 6: Peak Strain and Strain Rate Results

		Peak Strain		Peak Strain Rate	
Location		mean (με)	SD (±με)	mean (με)	SD (±με)
Simulated Staple (ST)	Max	543	165	7921	3249
	Min	-453	135	-3494	1206
	Shear	838	211	10390	4494
Anterior Medial (AM)	Max	488	175	6946	2510
	Min	-473	93	-3588	1221
	Shear	814	177	8612	3050
Anterior Lateral (AL)	Max	333	99	2748	1360
	Min	-620	169	-7282	2515
	Shear	914	260	9600	3344
Lateral (LA)	Max	287	78	2735	971
	Min	-708	206	-8555	3172
	Shear	954	259	11060	3773
Posterior Lateral (PL)	Max	271	62	2700	935
	Min	-766	192	-9703	2836
	Shear	1009	246	11837	3617
Posterior Medial (PM)	Max	533	137	7531	2758
	Min	-489	161	-3657	1303
	Shear	857	210	9909	3788

3.2.3 Intra-Subject Variability

The intra subject peak strains and strain rates showed noticeably smaller standard deviations than the inter-subject peak strains and strain rates. For example, the intra-subject peak strain standard deviations were an average of 87.37με lower than the inter-subject strains, and the strain rate standard deviations were an average of 779.8με/sec lower than the inter-subject strain rates. Intra-subject peak strains and strain rates are shown in Table B-1 in Appendix B.

In order to evaluate the variability of computed bone strain within a subject, the Coefficient of Multiple Correlation (CMC) was calculated for the strains at each location (AM, AL, LA, PL, PM, and ST) for individual subjects. The CMC was used to describe the repeatability of the strain curves for each subject. When the curves being compared are very similar, the CMC value approaches a value of one, while dissimilar curves approach a CMC of zero. The CMC values calculated for each subject are shown in Table 7.

Table 7: Coefficient of Multiple Correlation for Each Subject

Subject	Mean CMC
003	0.9262
006	0.9561
007	0.9371
013	0.9151
015	0.8579
016	0.9656
017	0.9396
018	0.8906
022	0.9233
023	0.9454
024	0.9239
026	0.9442

These results indicate that the assumption that a mean strain curve calculated from the 12 strides per subject can be used as the representative strain data from that subject is valid.

3.3 Expected Range of Strain and Strain Rate for the Tibial Mid-Shaft

The expected ranges determined by the bootstrap method and average values of the strain and strain rate for a gait cycle for the anterior medial location, the simulated staple, the anterior lateral location, the lateral location, the posterior lateral location, and the posterior medial location are shown in Figures 13 through 24, respectively.

The timing of the strain peaks occurred during consistent phases of the gait cycle. As seen in Figure 13 (below), the maximum shear strain at the anterior medial location had peaks just after heel strike (0 to 20% of the gait cycle), slightly prior to toe-off (40 to 50%), and following toe-off during the early swing phase (60 to 70%). The anterior lateral location and simulated staple (Figures 15 and 17) had similar peak locations to the anterior medial location. The maximum principal strain was similar at these locations with the exception of the absence of a peak prior to toe-off (40 to 50%), while the minimum principal strain showed a single peak late in the stance phase at toe-off (40 to 50%), coinciding with the second peak for the maximum shear strain. The timing of the peaks at the lateral (LA) and posterior lateral (PL) locations were less consistent, generally showing peaks near heel strike (0 to 20%) and toe-off (40 to 50%) for all three strains (maximum principal, minimum principal, and maximum shear) (Figures 19 and 21). Finally, the posterior medial (PM) location showed a definite peak following heel strike (0 to 20%) for the minimum principal and maximum shear strains, followed by smaller peaks at toe-off (40 to 60%) and early in the swing phase (60 to 65%) (Figure 23).

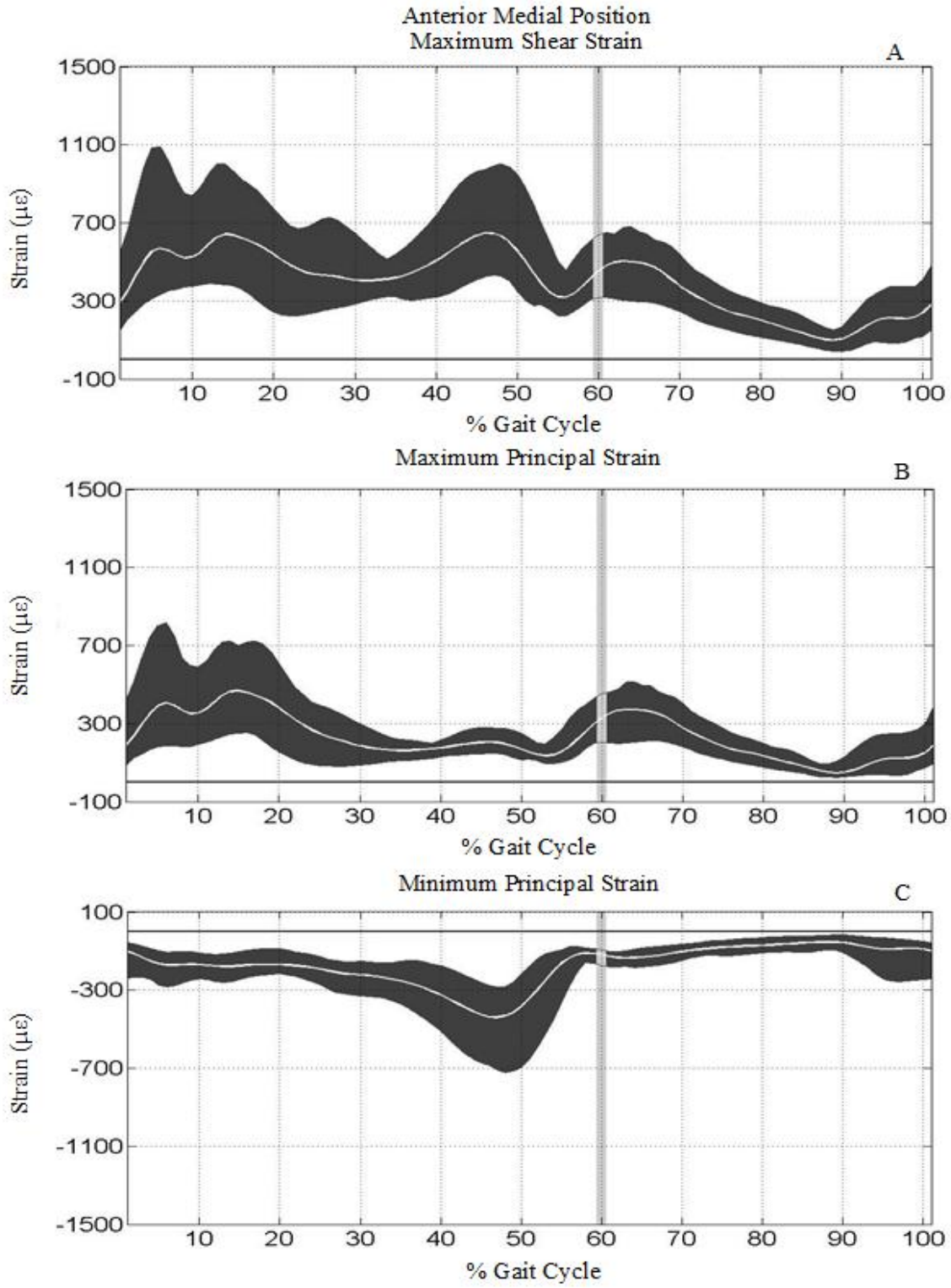

Figure 13: Expected Ranges of (A) Maximum Shear, (B) Maximum Principal, and (C) Minimum Principal Strains at the Anterior Medial Position on the Tibia. The vertical bands indicate the typical timing of toe-off.

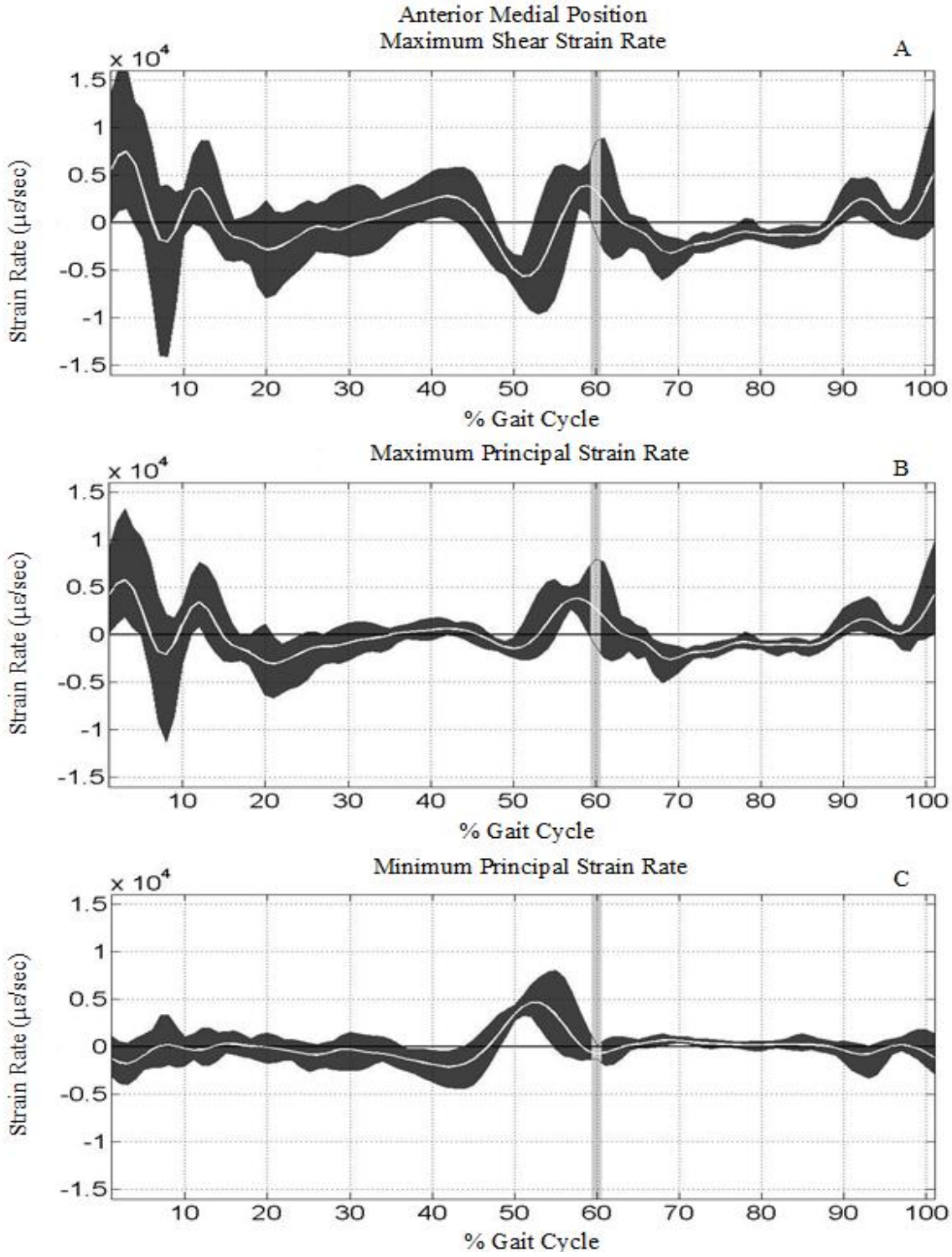

Figure 14: Expected Ranges of (A) Maximum Shear, (B) Maximum Principal, and (C) Minimum Principal Strain Rates at the Anterior Medial Position on the Tibia. The vertical bands indicate the typical timing of toe-off.

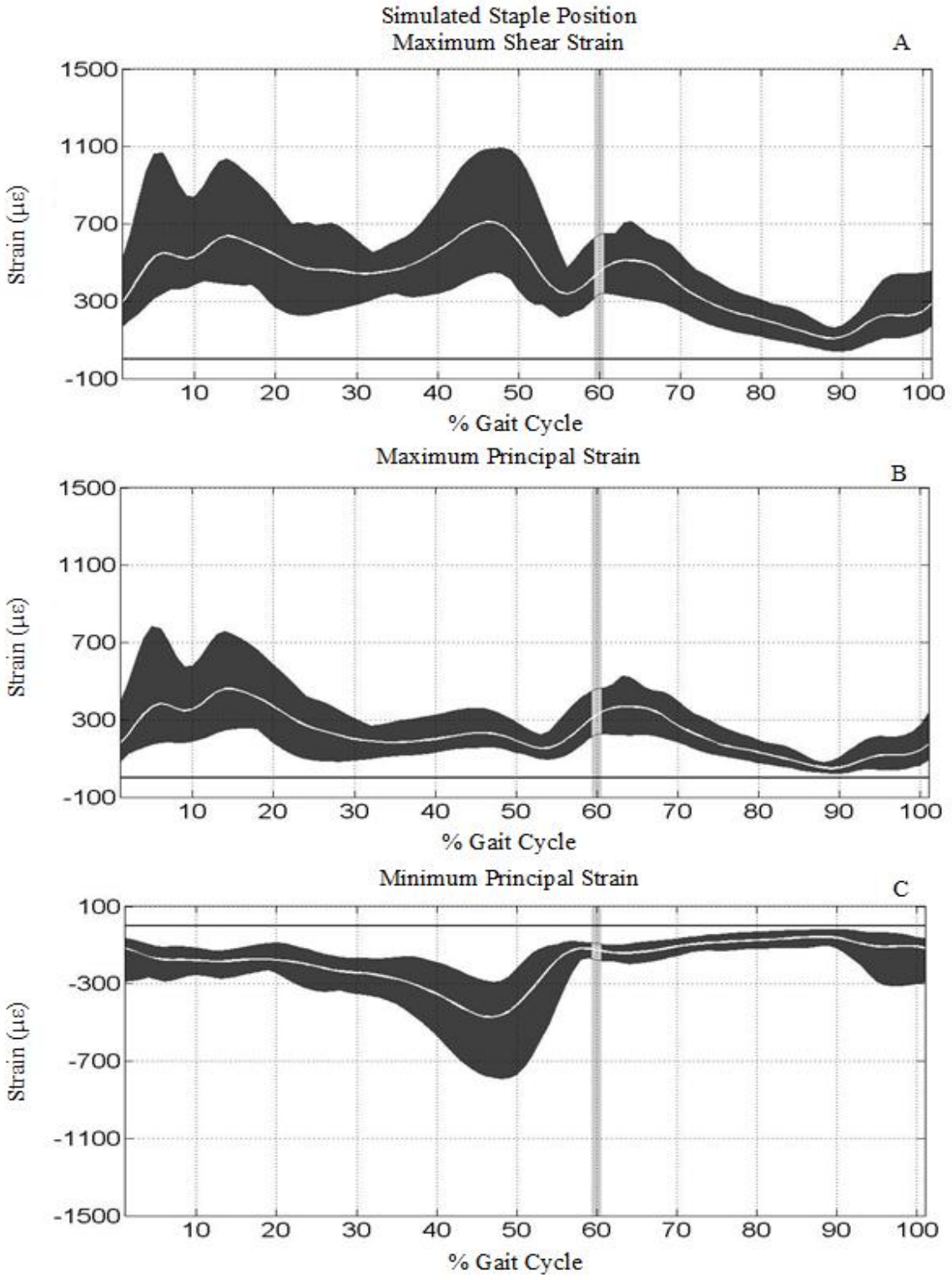

Figure 15: Expected Ranges of (A) Maximum Shear, (B) Maximum Principal, and (C) Minimum Principal Strains at the Simulated Staple Position on the Tibia. The vertical bands indicate the typical timing of toe-off.

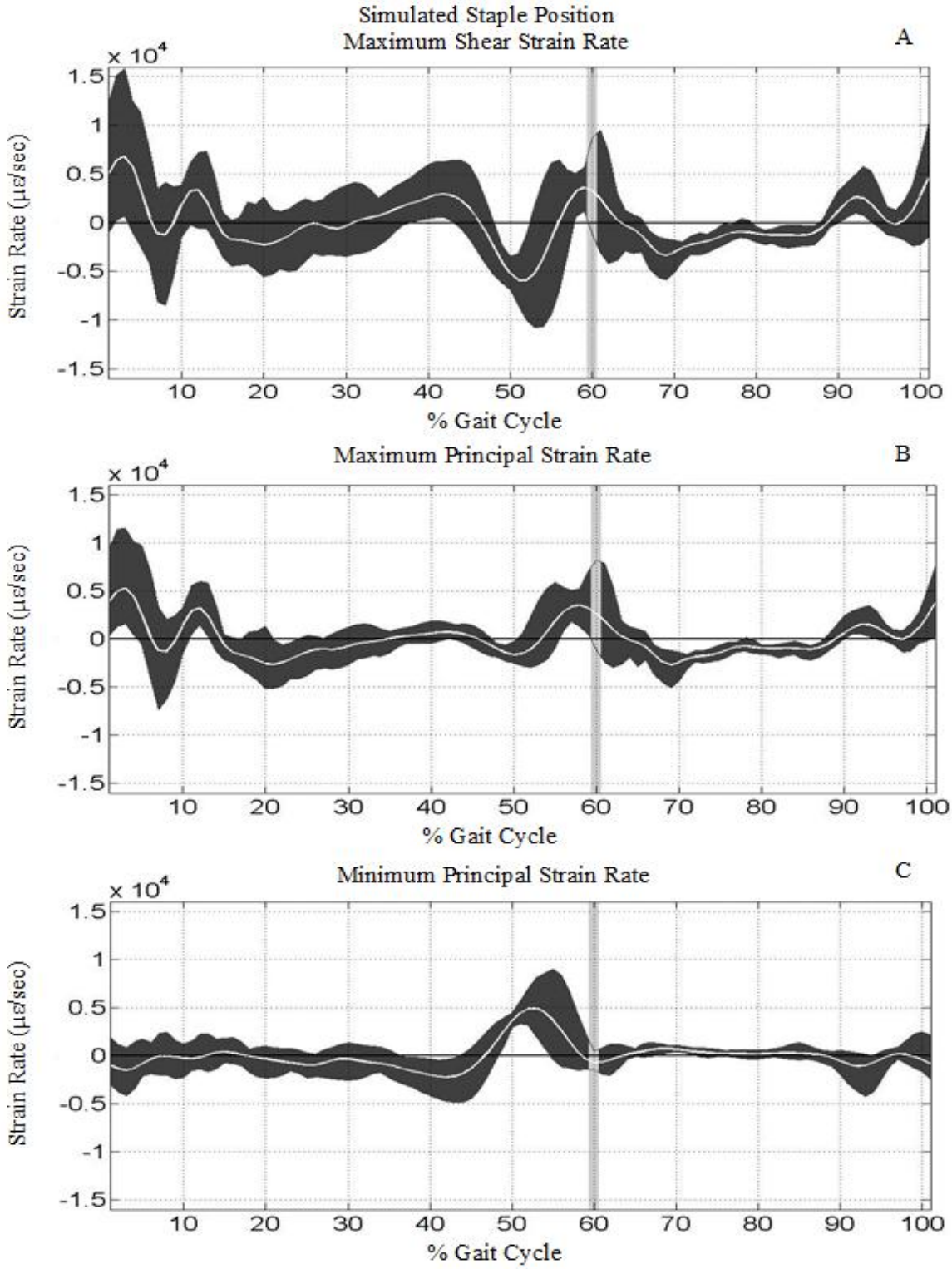

Figure 16: Expected Ranges of (A) Maximum Shear, (B) Maximum Principal, and (C) Minimum Principal Strain Rates at the Simulated Staple Position on the Tibia. The vertical bands indicate the typical timing of toe-off.

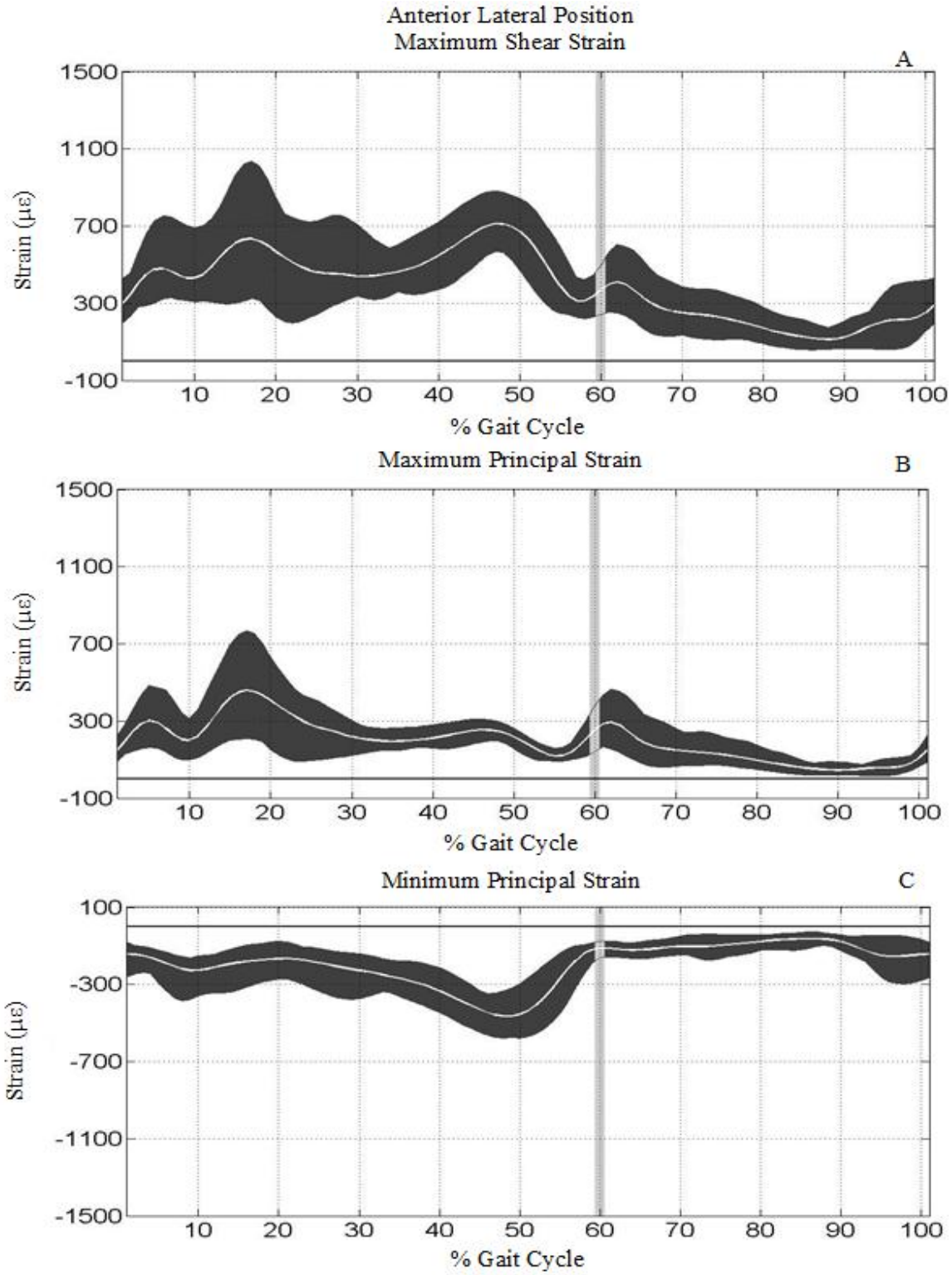

Figure 17: Expected Ranges of (A) Maximum Shear, (B) Maximum Principal, and (C) Minimum Principal Strains at the Anterior Lateral Position on the Tibia. The vertical bands indicate the typical timing of toe-off.

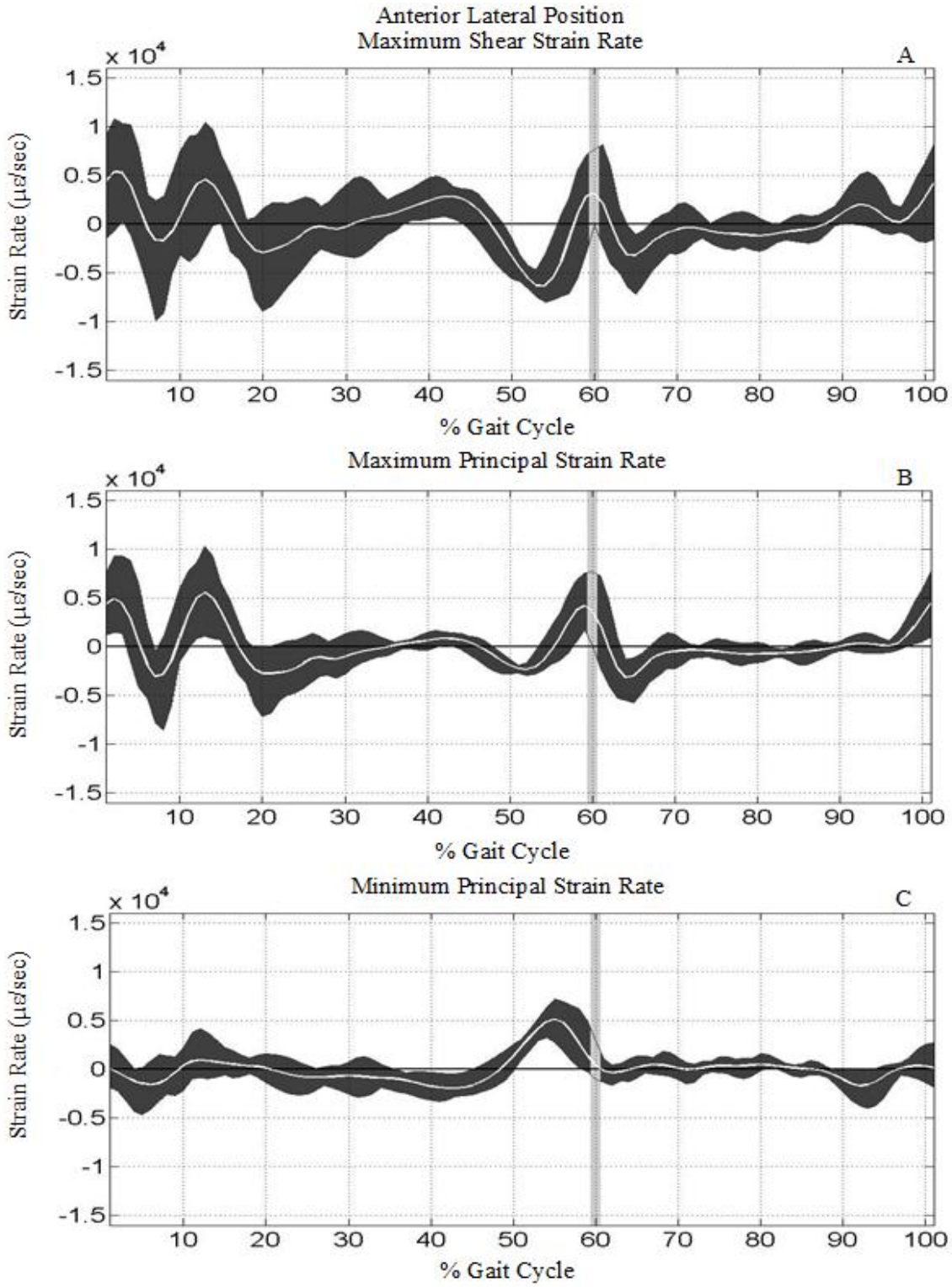

Figure 18: Expected Ranges of (A) Maximum Shear, (B) Maximum Principal, and (C) Minimum Principal Strain Rates at the Anterior Lateral Position on the Tibia. The vertical bands indicate the typical timing of toe-off.

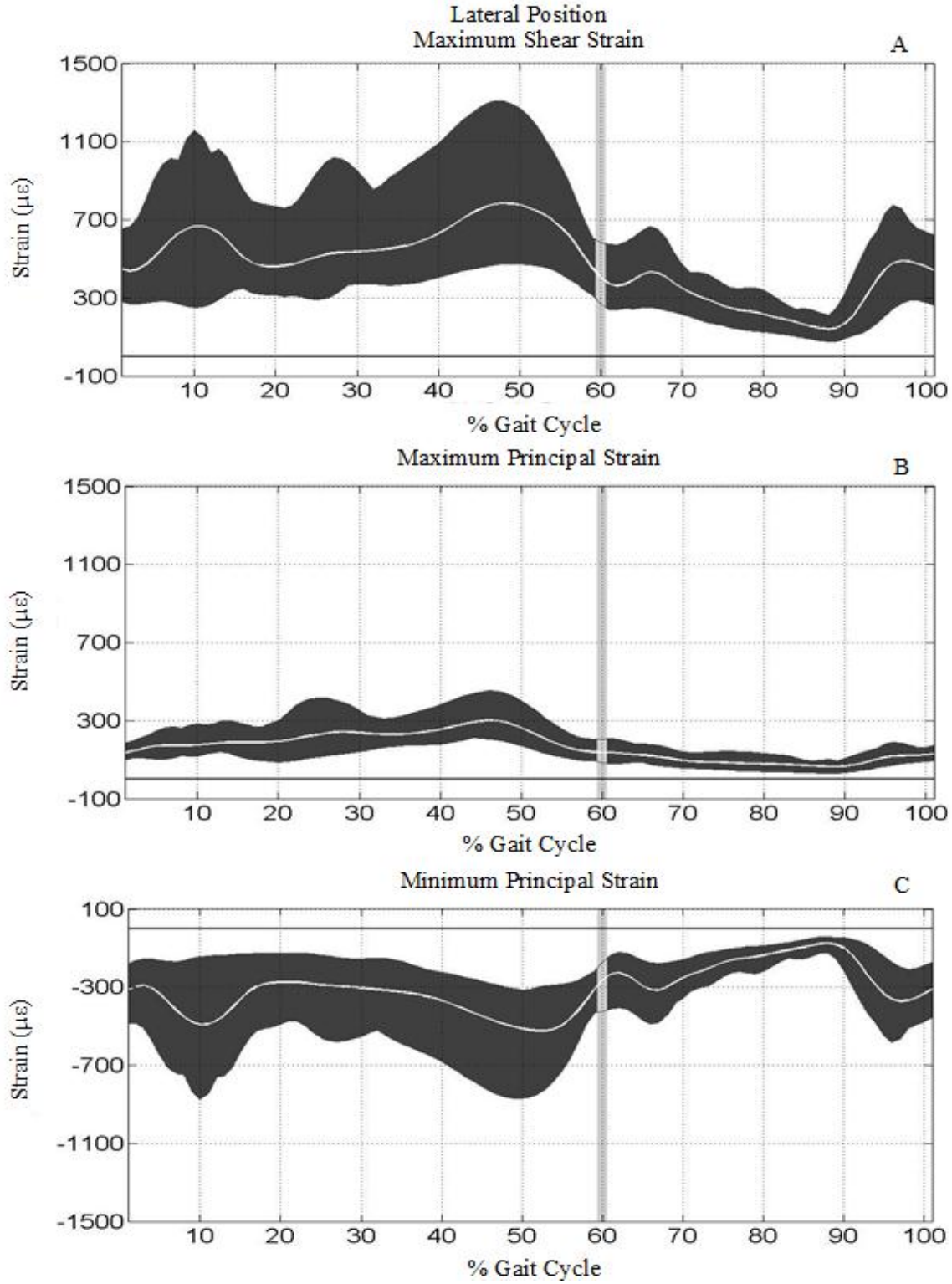

Figure 19: Expected Ranges of (A) Maximum Shear, (B) Maximum Principal, and (C) Minimum Principal Strains at the Lateral Position on the Tibia. The vertical bands indicate the typical timing of toe-off.

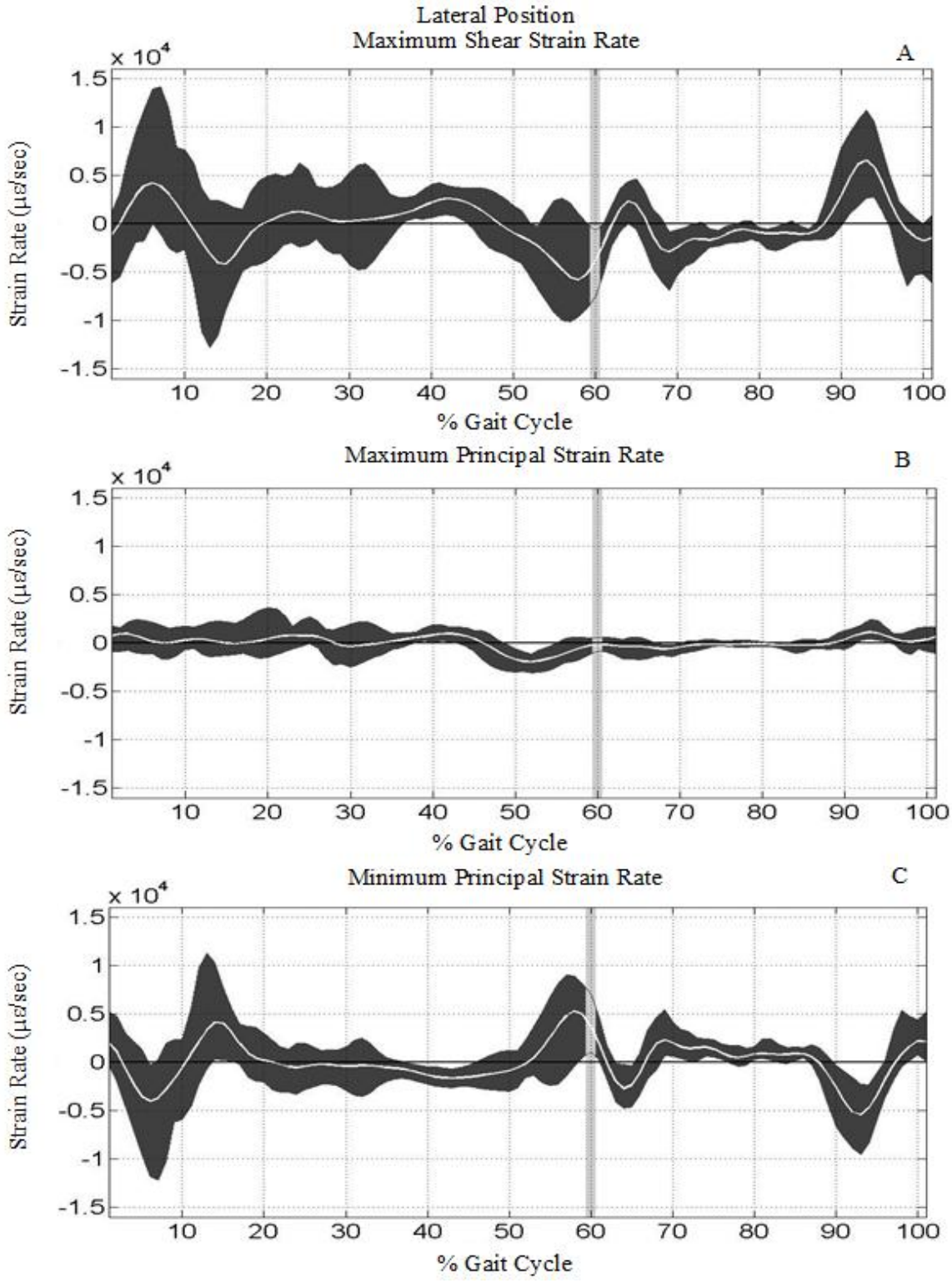

Figure 20: Expected Ranges of (A) Maximum Shear, (B) Maximum Principal, and (C) Minimum Principal Strain Rates at the Lateral Position on the Tibia. The vertical bands indicate the typical timing of toe-off.

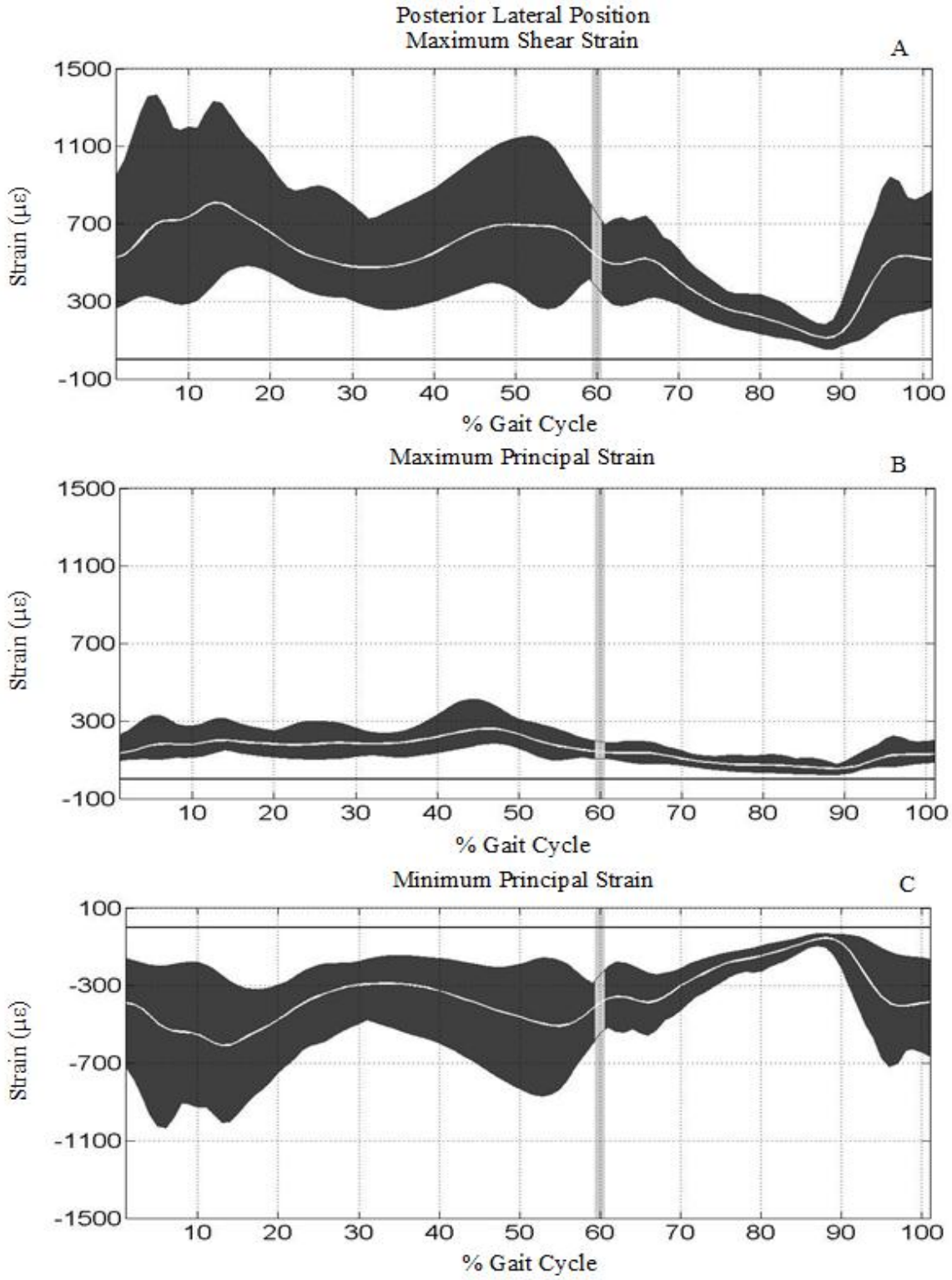

Figure 21: Expected Ranges of (A) Maximum Shear, (B) Maximum Principal, and (C) Minimum Principal Strains at the Posterior Lateral Position on the Tibia. The vertical bands indicate the typical timing of toe-off.

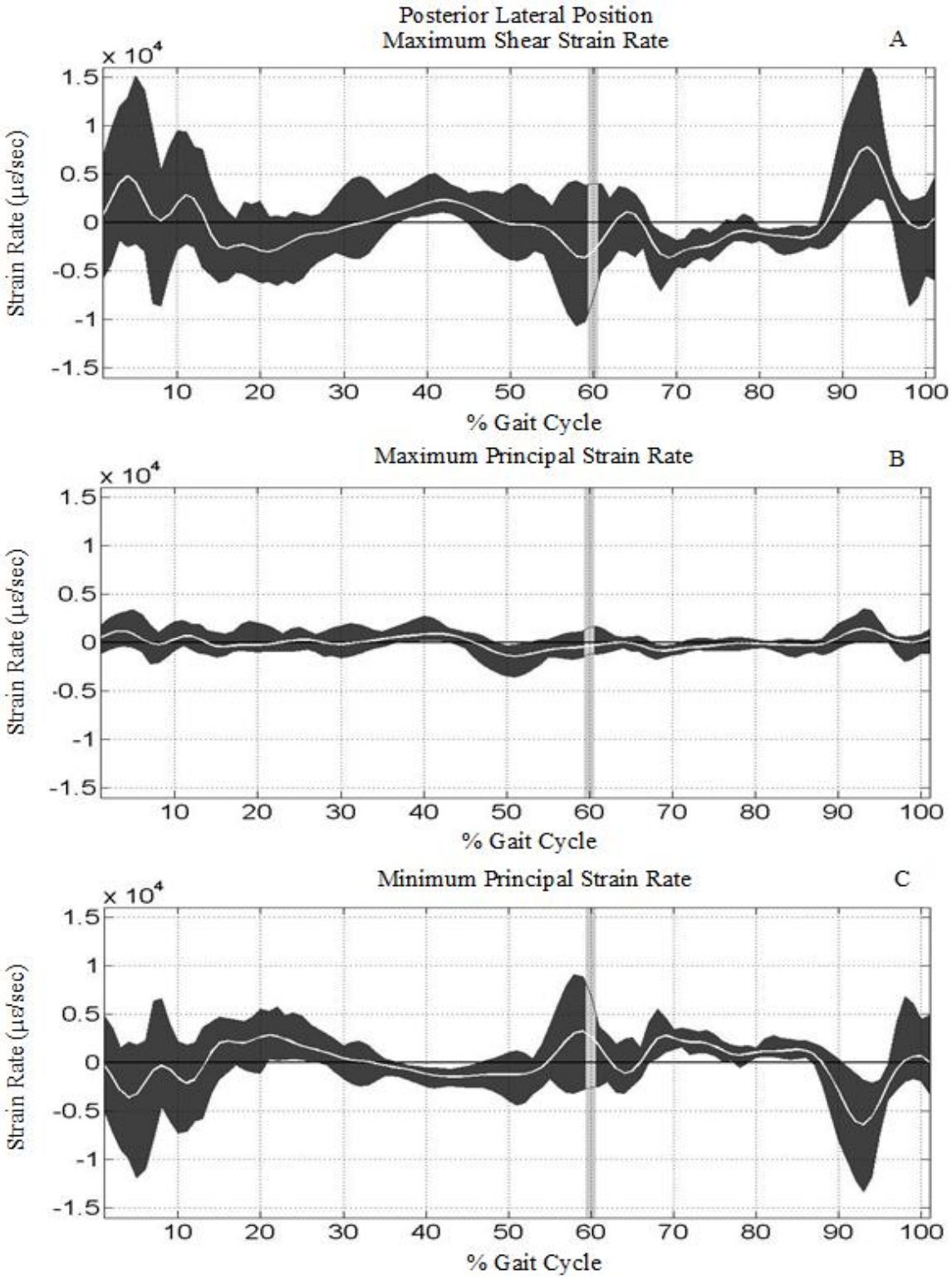

Figure 22: Expected Ranges of (A) Maximum Shear, (B) Maximum Principal, and (C) Minimum Principal Strain Rates at the Posterior Lateral Position on the Tibia. The vertical bands indicate the typical timing of toe-off.

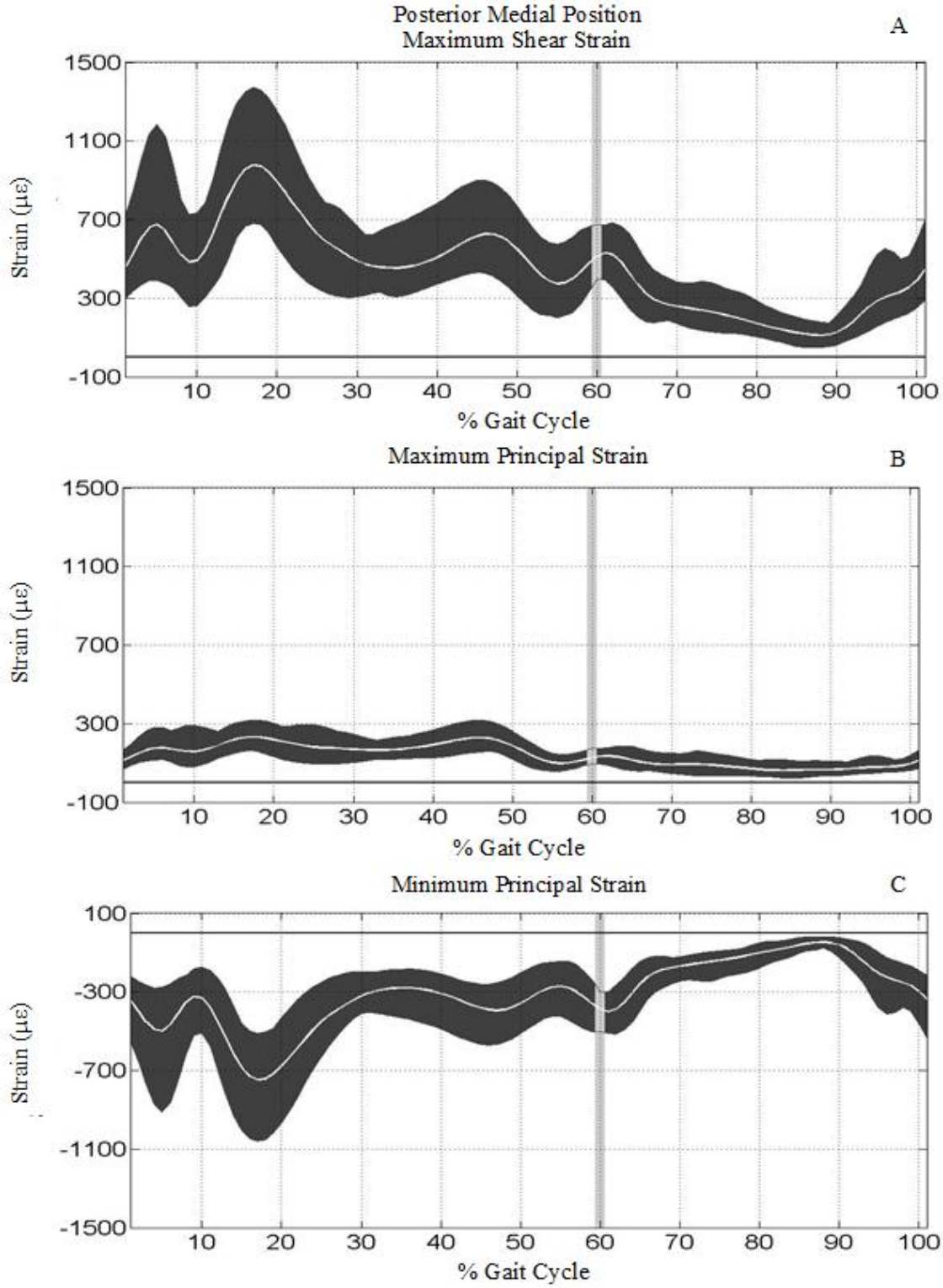

Figure 23: Expected Ranges of (A) Maximum Shear, (B) Maximum Principal, and (C) Minimum Principal Strains at the Posterior Medial Position on the Tibia. The vertical bands indicate the typical timing of toe-off.

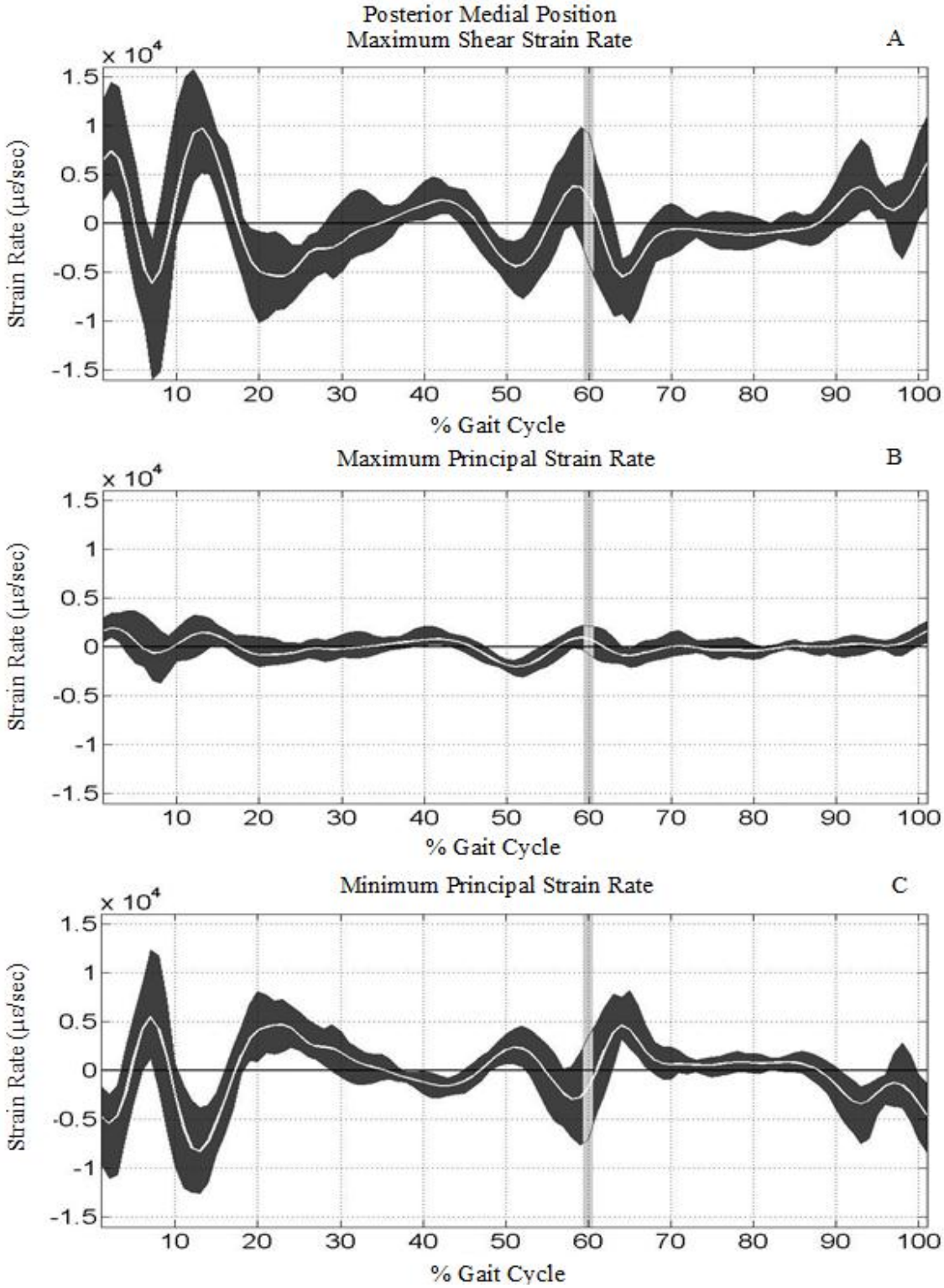

Figure 24: Expected Ranges of (A) Maximum Shear, (B) Maximum Principal, and (C) Minimum Principal Strain Rates at the Posterior Medial Position on the Tibia. The vertical bands indicate the typical timing of toe-off.

CHAPTER 4: DISCUSSION

The purpose of this study was to establish an expected range for tibial bone strain during walking for a homogeneous subject group. The expected ranges were generated from the 2.5 and 97.5 percentiles of a bootstrapped dataset. In addition to this overall goal, the inter-subject (between subjects) and intra-subject (within a single subject) variability of tibial bone strain and strain rate at various locations around the tibial mid-shaft were calculated. The noticeably larger standard deviation for the inter-subject strains and strain rates is understandable due to the use of subject specific bone geometry and material properties as well as the natural variability in the subjects' walking patterns and anthropometric proportions.

The ability to differentiate between normal tibial strain and strain rate levels and potentially harmful strain and strain rate levels is critical for research into tibial stress fracture development. The results from this study show that for a homogenous population the tibial strain and strain rate can vary substantially. The subjects analyzed in this study consisted of males in their twenties (mean: 20.85 years, SD: 1.5 years), with a body mass index below 28, and participating in recreational sports or exercise at least three times per week. The mean inter-subject standard deviation was 153με (averaged for the six locations of interest), with the highest variability in the shear strain at the posterior lateral (PL) location (SD: 245με) and least variability in the maximum shear strain at the posterior medial (PM) location (SD: 61με). For the duration of the gait cycle, the expected range of strains was wider at peak locations, indicating that there were differences in the timing and magnitude of peak strain and strain rate among subjects. While there was a sizeable amount of variability in the strain and strain rate peaks of the population, those peaks occurred during consistent phases of the gait cycle. The maximum

shear strain (see Figure 13A in Chapter 3) at the anterior-medial (AM) location had peaks just after heel strike (0 to 20% of the gait cycle), slightly prior to toe-off (40 to 50%), and following toe-off during the early swing phase (60 to 70%). The maximum principal strain (Figure 13 – B) was similar at these locations with the exception of the peak at toe-off (40 to 50%), while the minimum principal strain (Figure 13C) showed a single peak late in the stance phase near toe off (40 to 50%), coinciding with the second peak for the maximum shear strain.

The timing of these peak strains appears reasonable. During the loading response phase (0 to 20%), the anterior face of tibia is experiencing tensile loading, and the posterior face is experiencing compressive loading. The tensile load on the anterior aspect is partly due to the vertical (normal) ground reaction force (GRF) acting posterior of the neutral bending axis of the tibia and the anterior posterior (shear) GRF acting posteriorly on the foot early in the stance phase (resulting in a bending load on the tibia). In addition to the bending load caused by the reaction forces, the tibia is also experiencing loading from active muscles. During the loading response phase, the quadriceps muscles (vastus lateralis, vastus medialis, vastus intermedius, and rectus femoris) and the tibialis anterior are both actively applying force to the anterior face of the tibia (Anderson & Pandy, 2001; Sasaki & Neptune, 2010). The combination of the tensile bending load and the forces of the quadriceps muscles, tibialis anterior and other dorsiflexor muscles acting axially along the tibia results in a positive (tensile) strain, apparent in the maximum principal strain curve (Figure 13B). Due to the shape of the tibia, and the fact that the muscles do not only act axially along the tibia's longitudinal axis, the tensile bending load and muscle forces will also result in shear strains, which are apparent in Figure 13A. During mid-to-late stance phase (30 to 60%), the bending load changes directions due to the vertical GRF shifting anteriorly. The shift of the vertical GRF results in a compressive load on the anterior aspect of the tibia prior to toe-off. This bending load results in a negative strain (compressive) that is seen in the minimum principal strain curve (Figure 13C). During swing phase, the GRFs play no part

in the loading of the tibia, resulting in generally lower strains, which are caused by antagonistic muscle activity, and muscle activity in preparation for heel strike. The timing of the peaks for the anterior medial (AM) location and simulated staple are consistent with previous *in vivo* tibial strain research by Lanyon *et al.* (Lanyon et al., 1975). Using strain gauges at a similar location to the simulated staple, they found peaks at just after heel strike, just prior to toe-off, and early in swing phase (Lanyon et al., 1975)

The comparison between previous *in vivo* research and the results from this study were outlined in Table 5 (seen in Chapter 3). The maximum principal, minimum principal, and maximum shear strain results from this study differed from previous *in vivo* results by an average of 23%, 27%, and 9%, respectively, while the strain rate results differed by an average of 44%, 33%, and 46%. Although these differences may seem large, this study has demonstrated that there is a considerable amount of variability in the strains and strain rates even for a homogenous subject population. In fact, all *in vivo* peak strain results reported in previous studies were within the expected range for peak strains (Figure 25), and all *in vivo* peak strain rate results except for the results by Burr *et al.* (Burr et al., 1996) were within the expected range of peak strain rates (Figure 26). Therefore, the ranges of strain and strain rate obtained in this study may be applicable for a wider range of population. The sample population for this study consisted of males, 20.85 years $\pm$ 1.5 years old, with a BMI under 28, and physically active, while the subjects in those *in vivo* studies were four males and one female, aged 35, 39, 42, 49, and 33 (mean: 39.6 years, SD: $\pm$6.3 years) who were reported as being healthy and at least recreationally active.

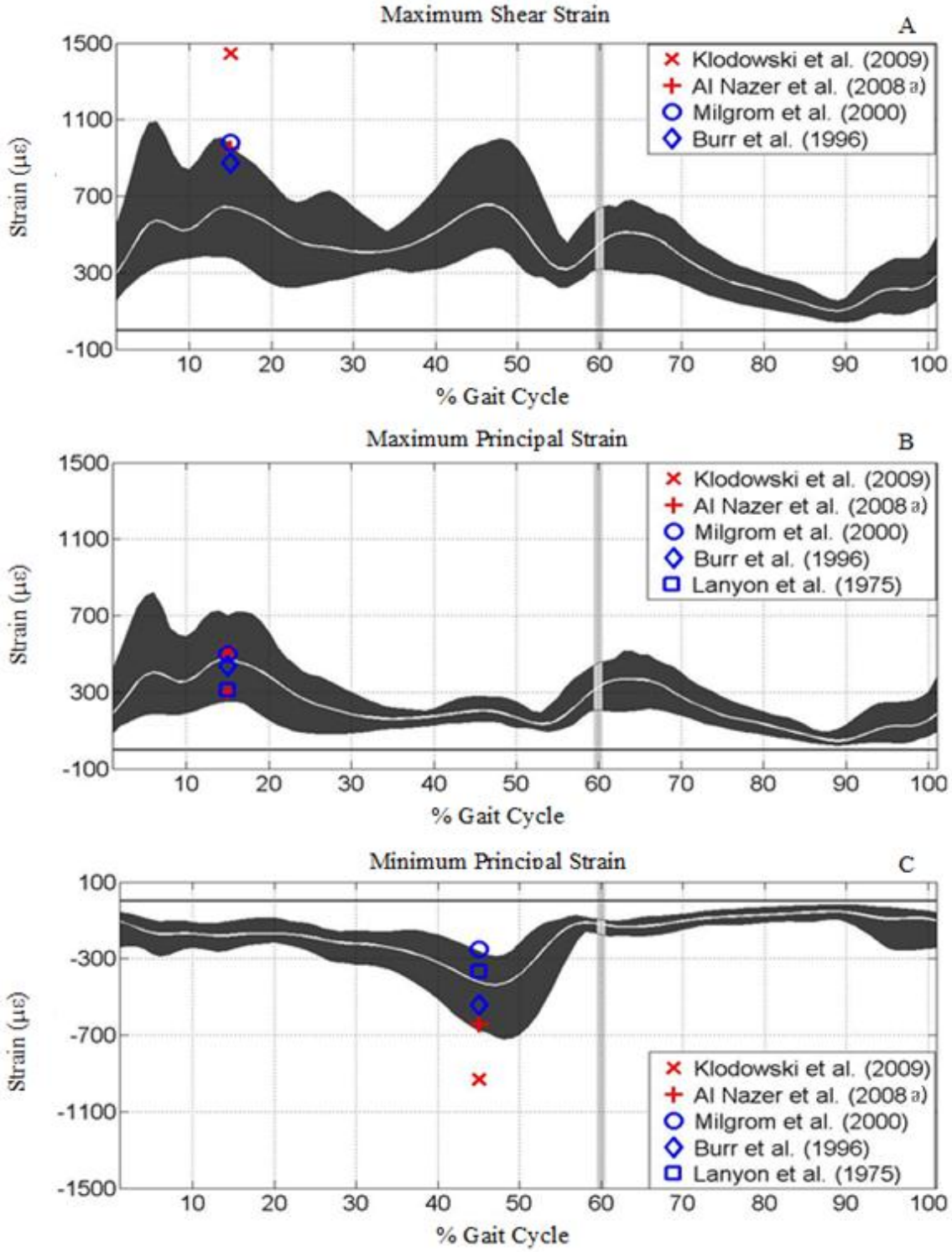

Figure 25: Maximum Shear (A) Maximum Principal (B) and Minimum Principal (C) Strains and previous research maximum values. The gray band represents toe - off. Peak *in vivo* strain results were assumed to occur at similar locations to the peak strain results in this study. The vertical bands indicate the typical timing of toe-off.

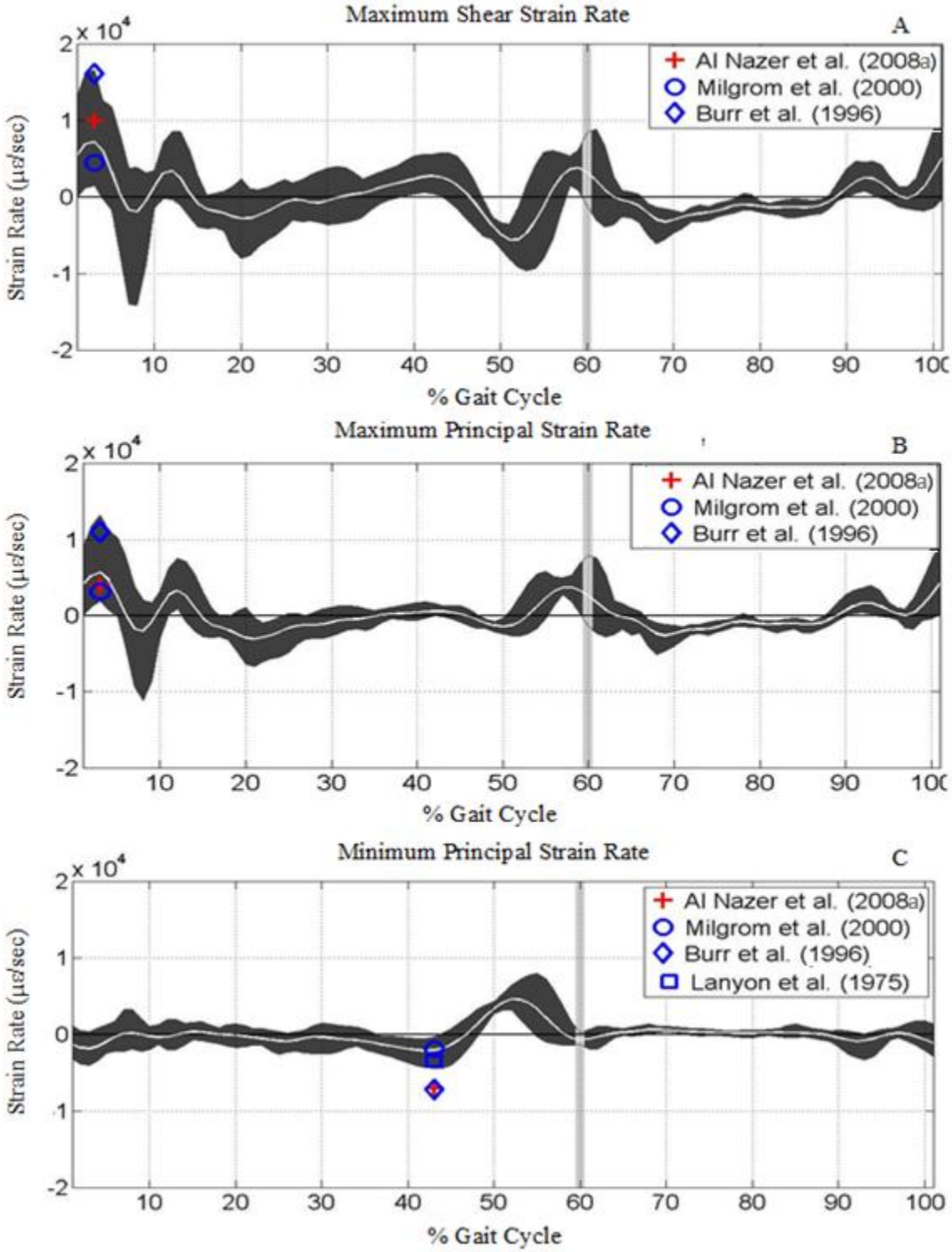

Figure 26: Maximum Shear (A) Maximum Principal (B) and Minimum Principal (C) Strain Rates and Previous Research Maximum Values. The gray band represents toe - off. Peak *in vivo* strain rate results were assumed to occur at similar locations to the peak strain results in this study. The vertical bands indicate the typical timing of toe-off.

As shown in Figure 25 above, the minimum principal, and maximum shear strain results reported by Klodowski *et al.* were well outside the expected ranges of strains in this study (Klodowski et al., 2009). While this study's minimum principal and maximum shear were much lower (49% and 44%, respectively) than those reported by Klodowski et al., the maximum principal strain was lower by only 5%. Compared to the results reported by Al Nazer et al., the strains from the present study were 37% higher (maximum principal strain), 27% lower (minimum principal strain), and 14% lower (maximum shear strain) (Al Nazer et al., 2008a). The strain values reported by Al Nazer et al. were within the expected range for the maximum principal, minimum principal, and maximum shear strains (Figure 25). There are several possible explanations for these differences, mostly due to methodological differences. First, Al Nazer *et al.* and Klodowski *et al.* both used simulated ground reaction forces (GRFs) in place of the experimental GRFs (Al Nazer et al., 2008a; Klodowski et al., 2009). The simulated GRFs used by Al Nazer *et al.* had an increased number of force peaks (i.e., high-frequency components) and increased magnitude (Figure 8 in Al Nazer et al., 2008a). The simulated GRFs used by Klodowski *et al*. showed an increased number of peaks for a single gait cycle, but failed to produce consistent magnitudes matching the experimental GRFs (Figure 5 in Klodowski et al., 2009). The experimental GRFs (see Figure A-1 in Appendix A) used for this study were much more consistent, resulting in a more reliable loading pattern for the dynamic simulations of walking. In addition to the simulated GRFs, Al Nazer *et al.* used a single material property for the entire tibia. The material property was considered to be linear elastic and transversely isotropic and based on literature values. This simplified model may cause an error in strain computation (Gray et al., 2008). The effect of using a single material property on the present model was investigated for a single subject. The maximum shear, maximum principal, and minimum principal strains (Figure 27) at the anterior medial location were compared using the 95% confidence interval of the mean strain, and a statistical significance was tested by comparing

the two 95% confidence intervals. A significant difference was shown by locations on the curve where the two intervals do not overlap. As shown below, the effect of the single material property was a significant increase in strain at all points of the gait cycle.

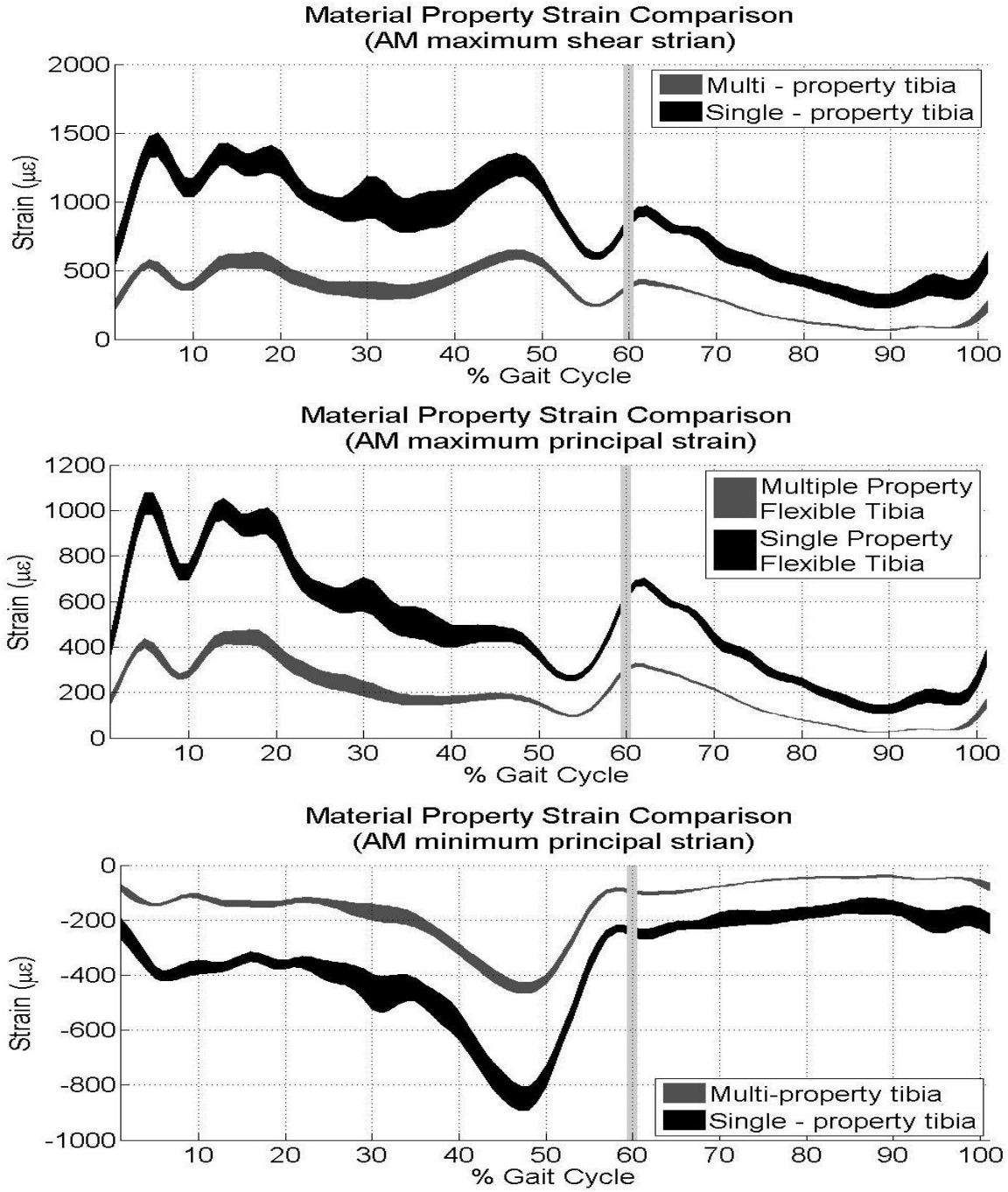

Figure 27: Single Material Property Versus Multiple Material Properties. The vertical bands indicate the typical timing of toe-off.

On top of using simulated GRFs, Klodowski *et al.* used different parameters for creating the musculoskeletal model and performing the dynamic simulation (Klodowski et al., 2009). First, they used a complete musculoskeletal model (upper and lower body), while the present study used only a lower body musculoskeletal model with prescribed kinematics at the mass center of the pelvis. Second, they used a muscle model consisting of open-loop simple muscles for the right leg tibialis anterior, soleus, rectus femoris, and the medial head of the gastrocnemius, closed-loop Hill-type muscles for the remaining muscles in the right leg, and closed-loop simple muscles (PID tuned actuators) for the remaining muscles in the model. The open-loop muscles used by Klodowski *et al.* were controlled by EMG activation patterns obtained during their experimental data collection. In contrast, the muscle model used in this study employed closed-loop simple muscles for a total of 15 muscles controlling the right shank and foot, and PID joint-torque actuators to control the left and right hip, the left knee and the left ankle. These differences in actuators can cause different forces applied to the flexible tibia, which could result in different strain magnitude.

4.1 Filtering Effects

In this study, the calculated tibial bone strain data were low-pass filtered because the raw strain data had noticeable high frequency components (Figure 28). These high frequency components were assumed to have originated from muscle forces because the muscle actuators were controlled by simple PID controllers.

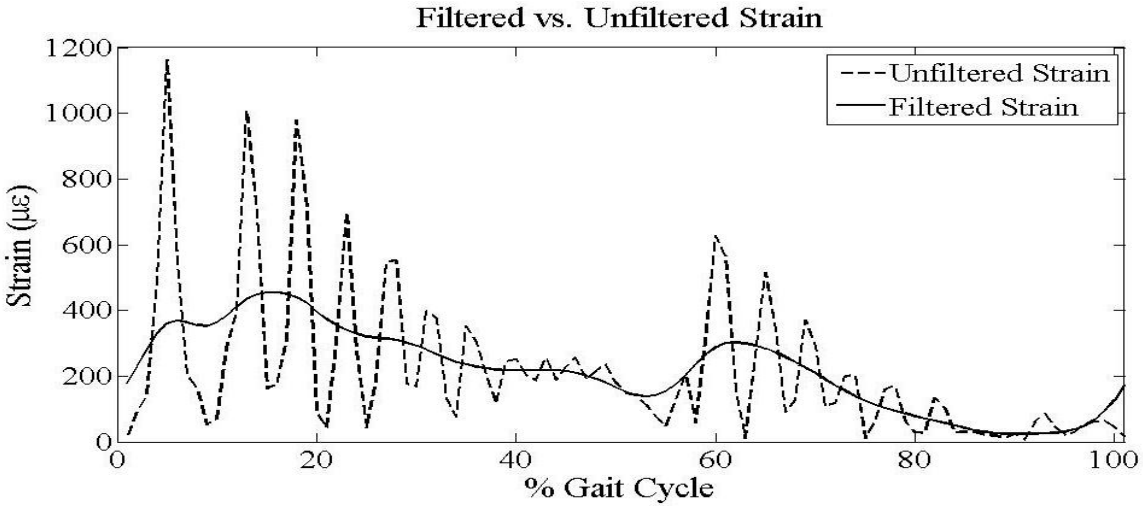

Figure 28: Filtered Versus Unfiltered Strain Curves for the Anterior Medial Location for a Representative Subject

In order to confirm this assumption, power spectrum analyses for the strain data (Figure 29) and for muscle forces (Figure 30) were performed. As shown in these figures, the frequency range of bone strain was correspondent with the frequency range of muscle forces.

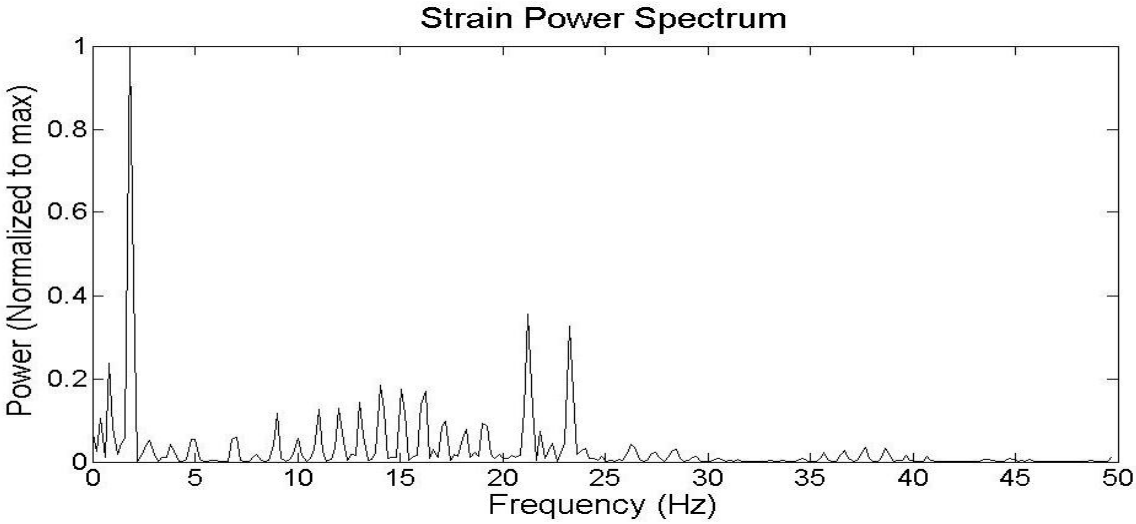

Figure 29: Power Spectrum for the Strain from a Representative Subject

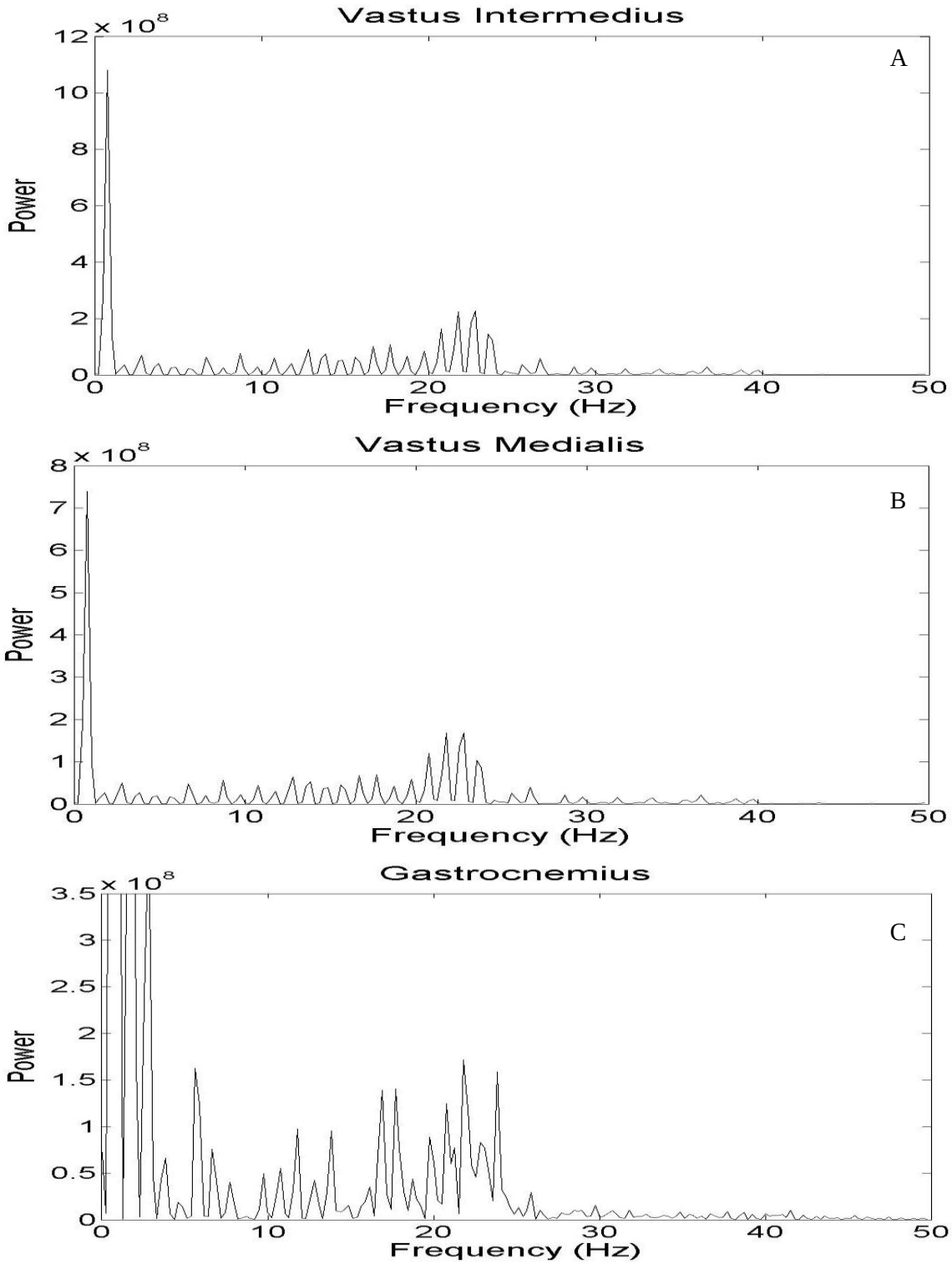

Figure 30: Power Spectrums for (A) vastus intermedius, (B) vastus medialis, (C) gastrocnemius, (D) hamstrings, (E) soleus, (F) tibialis posterior, and (G) extensor hallucis.

In this study, a low pass cut-off frequency of seven Hz was selected to smooth the raw bone strain data. However, the cut-off frequency could also influence the magnitude of strain or strain rate. Therefore, the sensitivity of the strain magnitude to the cut-off frequency was analyzed by filtering the data with three other cut-off frequencies (3, 5, and 16.04 Hz). 16.04 Hz is the highest frequency used in *in vivo* data (Burr et al., 1996). The results showed that the 5 and 7 Hz cutoff frequencies were able to reduce the noise substantially (unlike 16.04 Hz), while not reducing the peaks as occurred when using the 3 Hz cutoff frequency (Figure 31). When comparing the results with previous research, the 7 Hz cutoff frequency resulted in peak strains and strain rates that were closer to the *in vivo* studies (see Table 5 in Chapter 3) compared to the peaks when filtering with a 5 Hz cutoff frequency. The 95% confidence interval of the mean strain when using each of the cutoff filter frequencies is plotted in Figure 31. From these results, the cutoff frequency of 7 Hz used in this study appears the most appropriate. However, future studies may be able to fix this issue by using different muscle controllers (Hill – type or open – loop) or tuning the PID actuators for individual muscles, with the goal of reducing the noise in the main driving muscles. The peak values for the maximum principal, minimum principal, and maximum shear strains calculated at each cutoff frequency are outlined in Table 8.

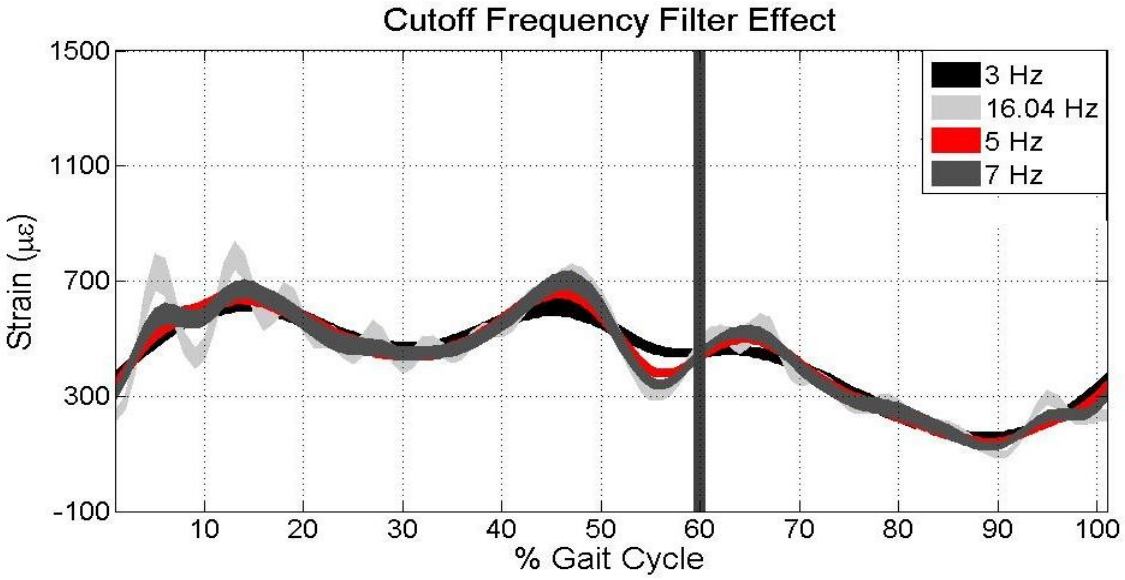

Figure 31: Cutoff Frequency Effect on Anterior Medial Maximum Principal Strain

Table 8: Effects of Filter Cutoff Frequency (Shown for the Anterior Medial Location)

	Peak Strain (με)			Peak Strain Rate (με/sec)		
Filter	Max Principal	Min Principal	Max Shear	Max Principal	Min Principal	Max Shear
3Hz filter[1]	468	-385	711	2986	-1684	4031
5Hz filter[1]	512	-432	784	5152	-2624	6786
7Hz filter[1]	552	-451	840	8010	-3525	10623
16.04Hz filter[2]	812	-490	1144	25261	-10063	33812
No filter	790	-536	1181	28304	-17295	40405
Percent difference 3Hz - 5 Hz	8	10	9	42	35	40
Percent difference 7Hz - 5 Hz	7	4	6	35	25	36
Percent difference 16.04Hz – 5 Hz	37	11	31	79	73	79
Percent difference No filter – 5 Hz	43	14	34	85	84	86

1 – Values chosen based on strain power spectrum (Figure 29)
2 – Highest reported cutoff frequency in *in vivo* data (Burr et al., 1996)

4.2 Limitations

There are several limitations to this study. First, the sample size might be small for establishing accurate expected ranges of tibial strains, although it is still larger than previous computational studies and *in vivo* studies. In order to approximate a larger sample size (and a normal distribution of subjects), the data from the 12 subjects were bootstrapped, resulting in a dataset that was much larger. The bootstrapped dataset resulted in marginally narrower expected ranges than the original dataset of 12 subjects. The differences between the results of this study and the results from a larger sample pool need to be evaluated in the future. Second, this study used a lower body musculoskeletal model to perform the dynamic simulation of walking. The lower body model required a motion tracker with a prescribed motion (based on the inverse kinematics) to complete the forward dynamics simulation. The lower body model was still able to recreate kinematics (see Figure 10 in Chapter 3) and reasonable joint kinetics (Figure 11). However, the prescribed pelvis kinematics could eliminate the influences associated with the upper body dynamics. Also, errors in the prescribed pelvis kinematics could load or unload the legs driven by joint and muscle actuators that track the experimental leg kinematics. The influences of these modeling and simulation techniques on strain computation need to be evaluated in the future. Finally, the relationships between bone density and Young's modulus used in this study could have a noticeable effect on the tibial bone strain. There are several relationships between bone density and Young's modulus that have been developed for different bone types and different bones. These relationships are outlined in a study performed by Helgason et al. (Helgason et al., 2008). In this study, the relationships for cortical and trabecular bone were selected based on the resulting Young's modulus for the cortical bone and trabecular bone, respectively, as well as the use of apparent density in the conversion (instead of ash density).

4.3 Delimitations

There are a few delimitations for this study. First, all subjects were male, aged 18 to 27, with a BMI under 28, and at least recreationally active. These subjects were selected as surrogate military recruits. Although the study results showed that the range of tibial strain obtained from these subjects included the variation of *in vivo* strain obtained from different adults (males and females with a mean age of 39.6) (Burr et al., 1996; Lanyon et al., 1975; C. Milgrom et al., 2000), the results should not be applied to estimate tibial strain among more diverse population such as children and impaired/injured individuals, or strain during different motor activities. Second, because stress fractures are not dependent on the strain or strain rate magnitude alone, these results should not be used as a range for predicting stress fractures, but as a base for comparing the strain results of future research.

4.4 Future Work

Future work using flexible bodies in dynamic simulations to determine strains should be directed toward methodological improvements and expanding the analysis to different types of activities. Due to the novelty of integrating a flexible tibia into a forward dynamics simulation to determine bone strain, the best practice for choosing the musculoskeletal model, muscle model, and type of muscle actuator have not been fully established. Future research improving these factors can improve the accuracy of strain and strain rate computations. The analysis techniques used in this study can be readily applied to different motor activities. The analysis of bone strains during more vigorous activities, such as running can provide valuable information about critical bone strain and strain rates that may be an important factor in causing stress fractures. Finally, investigating the contributing factors into what causes the inter-subject variability in bone strain may provide important information for both comparing the strains between subjects, and potential causes of stress fractures.

REFERENCES

Al Nazer, R., Klodowski, A., Rantalainen, T., Heinonen, A., Sievanen, H., & Mikkola, A. (2008a). Analysis of dynamic strains in tibia during human locomotion based on flexible multibody approach integrated with magnetic resonance imaging technique. *Multibody System Dynamics, 20*, 287-306.

Al Nazer, R., Rantalainen, T., Heinonen, A., Sievänen, H., & Mikkola, A. (2008b). Flexible multibody simulation approach in the analysis of tibial strain during walking. *J Biomech, 41*(5), 1036-1043.

Anderson, F. C., & Pandy, M. G. (2001). Dynamic optimization of human walking. *J Biomech Eng, 123*(5), 381-390.

Burr, D., Milgrom, C., Fyhrie, D., Forwood, M., Nyska, M., Finestone, A., et al. (1996). In vivo measurement of human tibial strains during vigorous activity. *Bone, 18*(5), 405-410.

Cheng, H., Obergefell, L., & Rizer, A. (1996). *The development of the GEBOD program*. Paper presented at the Biomedical Engineering Conference - Proceedings of the 1996 15th southern.

Craig, R., & Bampton, M. (1968). Coupling of Substructures for Dynamic Analysis. *AIAA Journal, 6*(7), 6.

Cram, J. R., Kasman, G.S., Holtz, J. (1998). *Introduction to Surface Myography* (1st ed.): Jones & Bartlett.

Ekenman, I., Halvorsen, K., Westblad, P., Felländer-Tsai, L., & Rolf, C. (1998). The reliability and validity of an instrumented staple system for in vivo measurement of local bone deformation. An in vitro study. *Scand J Med Sci Sports, 8*(3), 172-176.

Ekenman, I. M., Milgrom, C. M., Finestone, A. M., Begin, M. M., Olin, C. M., Arndt, T. P., et al. (2002). The Role of Biomechanical Shoe Orthoses in Tibial Stress Fracture Prevention. *Americal Journal of Sports Medicine, 30*(6), 866-870.

Frost, H. M. (1964). The Laws of Bone Structure. Springfield, IL.

Fyhrie, D., Milgrom, C., Hoshaw, S., Simkin, A., Dar, S., Drumb, D., et al. (1998). Effect of fatiguing exercise on longitudinal bone strain as related to stress fracture in humans. *Ann Biomed Eng, 26*(4), 660-665.

Gerstmayr, J., & Ambrosio, J. A. C. (2007). Component mode synthesis with constant mass and stiffness matrices applied to flexible multibody systems. *International Journal for Numerical Methods in Engineering, 2007*, 1518-1546.

Gray, H., Zavatsky, A., Cristofolini, L., & Gill, H. (2008). *Variation of Results with Number of Material Properties in a Human Tibia Finite Element Model*. Paper presented at the European Federation of National Associations of Orthopaedics and Traumatology (9th Congress).

Hansen, U., Zioupos, P., Simpson, R., Currey, J. D., & Hynd, D. (2008). The effect of strain rate on the mechanical properties of human cortical bone. *J Biomech Eng, 130*(1), 011011.

Helgason, B., Perilli, E., Schileo, E., Taddei, F., Brynjólfsson, S., & Viceconti, M. (2008). Mathematical relationships between bone density and mechanical properties: a literature review. *Clin Biomech (Bristol, Avon), 23*(2), 135-146.

Kadaba, M. P., Ramakrishnan, H. K., Wootten, M. E., Gainey, J., Gorton, G., & Cochran, G. V. (1989). Repeatability of kinematic, kinetic, and electromyographic data in normal adult gait. *J Orthop Res, 7*(6), 849-860.

Kaeding, C., & Najarian, R. (2010). Stress fractures: classification and management. *Phys Sportsmed, 38*(3), 45-54.

Kaminsky, L. A. (2006). *ACSM's resource manual for Guidelines for exercise testing and prescription* (5th ed.). Philadelphia: Lippincott Williams & Wilkins.

Klodowski, A., Rantalainen, T., Mikkola, A., Heinonen, A., & Sievanen, H. (2009). *A dynamic simulation of a human gait using the hybrid muscle model and a QCT-based flexible tibia.* Paper presented at the ASME International Design Engineering Technical Conferences and Computers and Information in Engineering Conference.

Lanyon, L. E., Hampson, W. G., Goodship, A. E., & Shah, J. S. (1975). Bone deformation recorded in vivo from strain gauges attached to the human tibial shaft. *Acta Orthop Scand, 46*(2), 256-268.

Lengsfeld, M., Schmitt, J., Alter, P., Kaminsky, J., & Leppek, R. (1998). Comparison of geometry-based and CT voxel-based finite element modelling and experimental validation. *Med Eng Phys, 20*(7), 515-522.

Li, L., & Caldwell, G. E. (1999). Coefficient of cross correlation and the time domain correspondence. *J Electromyogr Kinesiol, 9*(6), 385-389.

Linde, F., Hvid, I., & Madsen, F. (1992). The effect of specimen geometry on the mechanical behaviour of trabecular bone specimens. *J Biomech, 25*(4), 359-368.

Lisková, M., & Hert, J. (1971). Reaction of bone to mechanical stimuli. 2. Periosteal and endosteal reaction of tibial diaphysis in rabbit to intermittent loading. *Folia Morphol (Praha), 19*(3), 301-317.

Martin, R. B. (2001). *Musculoskeletal Fatigue and Stress Fractures.* New York: CRC Press.

Mendelson, S. B., Milgrom, C. M., Fineston, A. M., Lewis, J. B. M., Ronen, M. B., Burr, D. P., et al. (1998). Effect of Cane Use on Tibial Strain and Strain Rates. *American Journal of Physical Medicin & Rehabilitation, 77*(4), 333-338.

Milgrom, C., Finestone, A., Hamel, A., Mandes, V., Burr, D., & Sharkey, N. (2004). A comparison of bone strain measurements at anatomically relevant sites using surface gauges versus strain gauged bone staples. *J Biomech, 37*(6), 947-952.

Milgrom, C., Finestone, A., Segev, S., Olin, C., Arndt, T., & Ekenman, I. (2003). Are overground or treadmill runners more likely to sustain tibial stress fracture? *Br J Sports Med, 37*(2), 160-163.

Milgrom, C., Finestone, A., Simkin, A., Ekenman, I., Mendelson, S., Milgrom, M., et al. (2000). In vivo strain measurements to evaluate the strengthening potential of exercises on tibial bone. *The Journal of Bone and Joint Surgery, 82-B*(4).

Milgrom, C., Radeva-Petrova, D. R., Finestone, A., Nyska, M., Mendelson, S., Benjuya, N., et al. (2007). The effect of muscle fatigue on in vivo tibial strains. *J Biomech, 40*(4), 845-850.

Morgan, E., Bayraktar, H., & Keaveny, T. (2003). Trabecular bone modulus-density relationships depend on anatomic site. *J Biomech, 36*(7), 897-904.

Rathnayaka, K., Sahama, T., Schuetz, M., & Schmutz, B. (2010). Effects of CT image segmentation methods on the accuracy of long bone 3D reconstructions. *Med Eng Phys*.

Rubin, C. T., & McLeod, K. J. (1994). Promotion of bony ingrowth by frequency-specific, low-amplitude mechanical strain. *Clin Orthop Relat Res*(298), 165-174.

Sasaki, K., & Neptune, R. R. (2010). Individual muscle contributions to the axial knee joint contact force during normal walking. *J Biomech, 43*(14), 2780-2784.

Schileo, E., Taddei, F., Malandrino, A., Cristofolini, L., & Viceconti, M. (2007). Subject-specific finite element models can accurately predict strain levels in long bones. *J Biomech, 40*(13), 2982-2989.

Snyder, S. M., & Schneider, E. (1991). Estimation of mechanical properties of cortical bone by computed tomography. *J Orthop Res, 9*(3), 422-431.

Taddei, F., Schileo, E., Helgason, B., Cristofolini, L., & Viceconti, M. (2007). The material mapping strategy influences the accuracy of CT-based finite element models of bones: an evaluation against experimental measurements. *Med Eng Phys, 29*(9), 973-979.

Takeda, T., Narita, T., & Ito, H. (2004). Experimental study on the effect of mechanical stimulation on the early stage of fracture healing. *J Nippon Med Sch, 71*(4), 252-262.

TC, H. (1998). *Simulation and Bootstrapping for Teaching Statistics.* Paper presented at the American Statistical Association Preceedings of the Section on Statistical Education.

Thompson, D. (1961). On Growth and Form (Abridged Edition) (Vol. (Originally published 1917)): Cambridge Press.

Turner, C. H., Yoshikawa, T., Forwood, M. R., Sun, T. C., & Burr, D. B. (1995). High frequency components of bone strain in dogs measured during various activities. *J Biomech, 28*(1), 39-44.

Whiting, W. C., & Zernicke, R. F. (1998). *Biomechanics of musculoskeletal injury*. Champaign, IL: Human Kinetics.

Zioupos, P., Hansen, U., & Currey, J. D. (2008). Microcracking damage and the fracture process in relation to strain rate in human cortical bone tensile failure. *J Biomech, 41*(14), 2932-2939.

APPENDIX A

Experimental GRFs Used in the Forward Dynamics Simulation of Walking

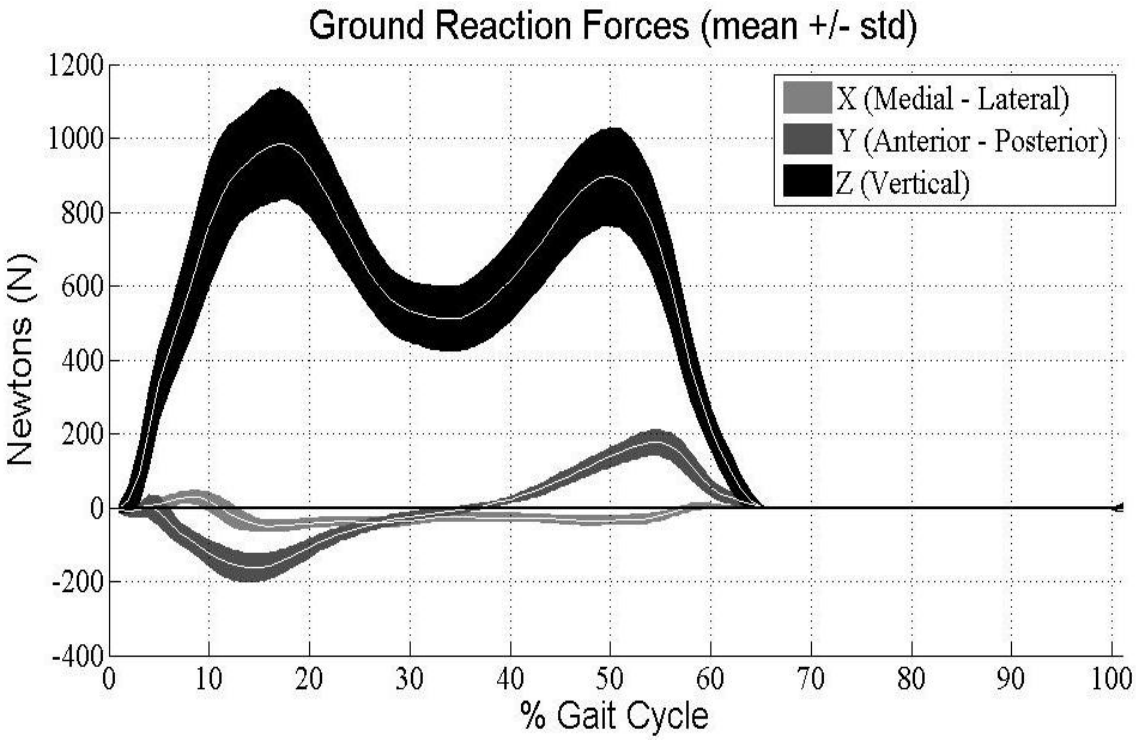

Figure A-1: Experimental GRFs Used in the Forward Dynamics Simulation of Walking.

APPENDIX B

Intra-Subject Mean and Standard Deviation for Maximum Principal, Minimum Principal, and Maximum Shear Strain

Table B-1: Intra-Subject Mean and Standard Deviation for Maximum Principal, Minimum Principal and Maximum Shear Strain

		Anterior Medial			Staple				
		Shear	Min	Max	Shear	Min	Max		
003	mean	813.95	-473.18	487.93	838.37	-453.52	543.15	mean	003
	st dev	177.07	92.912	174.71	210.53	135.44	164.53	st dev	
006	mean	686.93	-358.46	395.03	733.03	-372.88	474.51	mean	006
	st dev	85.021	52.054	35.262	115.07	56.487	64.713	st dev	
007	mean	908.92	-512.01	691.31	991.45	-698.79	520.39	mean	007
	st dev	48.308	47.438	26.07	145.42	76.069	28.812	st dev	
013	mean	706.09	-435.61	333.02	585.75	-398.67	332.33	mean	013
	st dev	73.176	39.446	17.672	57.452	31.14	22.283	st dev	
015	mean	1068	-507.42	776.16	901.06	-435.67	658.12	mean	015
	st dev	206.29	18.177	128.02	172.97	21.389	114.79	st dev	
016	mean	1010.1	-575.98	597.34	1155	-394.21	814.16	mean	016
	st dev	165.4	84.638	41.611	97.93	119.11	54.137	st dev	
017	mean	800.36	-401.05	561.39	688.58	-289.04	446.69	mean	017
	st dev	70.689	27.994	40.598	64.976	21.669	32.403	st dev	
018	mean	738.97	-435.36	564.97	788.75	-353.66	593.55	mean	018
	st dev	51.396	13.381	32.093	66.223	26.849	39.011	st dev	
022	mean	761.08	-376.53	497.67	830.18	-467.49	584.58	mean	022
	st dev	221.47	65.764	103.34	157.68	39.851	78.317	st dev	
023	mean	853.45	-582.9	311.02	1003.9	-723.1	464.15	mean	023
	st dev	96.812	43.574	41.061	86.501	49.811	13.662	st dev	
024	mean	896.77	-582.18	599.55	1084.5	-395.29	827.69	mean	024
	st dev	87.531	40.65	68.505	166.37	47.499	94.081	st dev	
026	mean	765.03	-529.01	261.4	658.39	-465.43	347.15	mean	026
	st dev	48.32	23.136	28.35	43.338	26.822	19.439	st dev	
Total	mean	571.66	-381.62	266.34	639.88	-447.95	454.51	mean	Total
	st dev	94.577	49.25	41.945	77.463	40.879	54.863	st dev	

Table B-1: Intra-Subject Mean and Standard Deviation for Maximum Principal, Minimum Principal and Maximum Shear Strain

		Lateral			Anterior Lateral				
		Shear	Min	Max	Shear	Min	Max		
003	mean	953.75	-708.22	286.94	914.14	-619.83	333.28	mean	
	st dev	258.91	206.14	78.17	259.98	168.67	99.302	st dev	
006	mean	906.82	-691.92	259.01	808.63	-533.7	302.26	mean	
	st dev	100.55	74.525	41.752	101.04	45.954	50.158	st dev	
007	mean	862.72	-546.21	419.71	735.61	-404.25	402.03	mean	
	st dev	167.53	43.504	89.217	203.26	41.48	75.343	st dev	
013	mean	778.43	-592.99	257	820.38	-530.59	311.13	mean	
	st dev	41.819	32.16	25.569	90.731	38.647	30.631	st dev	
015	mean	1221.8	-943.93	295.53	1162.2	-876.11	293.92	mean	
	st dev	227.55	178.72	16.106	188.92	153.08	17.323	st dev	
016	mean	1442.9	-1088.1	380.92	1269.7	-832.18	430.63	mean	
	st dev	102.06	75.398	60.734	268.67	95.162	136.53	st dev	
017	mean	946.23	-721.9	249.65	872.01	-633.98	278.27	mean	
	st dev	68.586	49.863	16.768	51.519	33.033	23.505	st dev	
018	mean	1017.2	-776.64	269.85	889.46	-619.87	306.24	mean	
	st dev	78.319	58.894	15.891	27.633	22.838	17.365	st dev	
022	mean	842.04	-588.39	326.8	873.5	-506.03	438.99	mean	
	st dev	229.82	121.67	92.79	348.74	142.33	141.74	st dev	
023	mean	552.66	-369.92	189.37	744.18	-519.85	286.15	mean	
	st dev	46.878	24.286	17.242	76.138	49.072	52.369	st dev	
024	mean	1213.7	-926.59	323.52	1315	-873.95	454.52	mean	
	st dev	74.215	57.963	30.524	128.52	58.124	52.641	st dev	
026	mean	863.87	-647.81	236.45	829.71	-611.49	275.36	mean	
	st dev	72.699	53.889	30.439	29.025	17.443	34.374	st dev	
Total	mean	796.73	-604.31	235.45	649.21	-495.94	219.89	mean	
	st dev	73.135	60.655	44.409	75.615	56.907	35.701	st dev	

Table B-1: Intra-Subject Mean and Standard Deviation for Maximum Principal, Minimum Principal and Maximum Shear Strain

		Posterior Lateral			Posterior Medial			
		Max	Min	Shear	Max	Min	Shear	
003	mean	271.28	-765.64	1009.4	533.39	-488.63	857.46	
	st dev	62.011	191.75	246.34	137.2	161.14	210.18	
006	mean	275.03	-700.09	952.34	510.29	-381.16	757.3	
	st dev	32.353	65.645	80.921	82.867	61.95	116.12	
007	mean	335.14	-1065	1377.9	530.31	-793.6	1109	
	st dev	26	32.56	44.599	34.099	71.711	137.48	
013	mean	238.47	-593.56	778.87	375.11	-394.29	583.28	
	st dev	24.512	45.537	51.276	29.937	30.492	54.556	
015	mean	299.49	-895.71	1163.7	686.4	-481.93	950.21	
	st dev	40.492	123.08	157.51	141.51	22.158	170.57	
016	mean	341.77	-991.31	1312.6	817.02	-389.54	1139.7	
	st dev	50.658	50.967	81.567	52.83	110.99	87.707	
017	mean	258.06	-841.25	1094.8	486.41	-295.42	732.5	
	st dev	13.163	57.075	73.33	42.425	21.969	70.114	
018	mean	227.18	-761.17	984.57	570.1	-381.81	764.45	
	st dev	9.455	50.409	63.132	46.724	32.76	66.231	
022	mean	316.41	-683.08	953.74	546.6	-575.56	934.94	
	st dev	68.296	67.221	151.16	114.82	45.698	184.12	
023	mean	252.47	-605.2	805.35	477.87	-792.95	1096.4	
	st dev	33.13	43.45	77.219	15.769	51.759	89.008	
024	mean	327.85	-991.17	1288.4	574.36	-441.43	879.18	
	st dev	38.24	89.604	113.49	70.647	70.23	101.42	
026	mean	198.95	-513.43	687.92	374.3	-476.61	687.74	
	st dev	28.521	48.653	65.011	26.88	33.263	59.278	
Total	mean	184.58	-546.62	712.77	451.91	-459.29	654.79	
	st dev	30.252	48.948	63.419	66.963	44.559	83.065	